

Mapping magnetic sources at the millimeter to micrometer scale in dunite and serpentinite by high-resolution magnetic microscopy

Zeudia Pastore^{1*}, Suzanne A. McEnroe¹, Geertje ter Maat¹, Hirokuni Oda², Nathan S. Church¹ and Patrizia Fumagalli³.

¹ Norwegian University of Science and Technology (NTNU), Department of Geoscience and Petroleum, Trondheim, Norway.

² Geological Survey of Japan, National Institute of Advanced Industrial Science and Technology (AIST), Tsukuba, Japan.

³ University of Milan, Department of Earth Sciences “Ardito Desio”, Milan, Italy.

* Corresponding author mail: zeudia.pastore@ntnu.no

Keywords: Magnetic anomalies; Scanning magnetic microscopy; Serpentinization; Dunite; Forward and inverse modeling; Natural remanent magnetization.

ABSTRACT

1 Rock samples can have wide range of magnetic properties depending on composition, amount of ferromagnetic
2 minerals, grain sizes and microstructures. Here, we used scanning magnetic microscopy, a highly sensitive and
3 high-resolution magnetometric technique to map remanent magnetic fields over a planar surface of a rock sample.
4 The technique allows for the investigation of discrete magnetic mineral grains, or magnetic textures and structures
5 with submillimeter scale resolution. Here, we present a case-study of magnetic scans of pristine and serpentized
6 dunite thin sections from the Reinfjord Ultramafic Complex, in northern Norway. The magnetic mineralogy is
7 characterized by electron microprobe, scanning electron- and optical-microscopy, and with rock magnetic
8 methods. In serpentized samples the magnetic carrier is end-member magnetite occurring as large discrete
9 grains and small grains in micron scale veins. By contrast, the pristine dunite sample contains large Cr-spinel
10 grains with very fine equant exsolutions ranging in composition from ferrichromite to end-member magnetite.
11 Forward and inverse modeling of the magnetic anomalies is used to determine the remanent magnetization
12 directions and intensities of discrete magnetic sources observed in the scanning magnetic microscopy. The fine-
13 scale magnetization of the rock sample is used to investigate the magnetic carriers and the effect of
14 serpentization on the magnetic properties of the dunite. Modeling shows that the dipolar magnetic anomalies
15 that are mapped by scanning magnetic microscopy are caused by grains with heterogeneous magnetic sources.
16 The intensity of the magnetization and the amount of magnetic minerals are higher in the serpentized sample
17 than the pristine dunite sample, consistent with the measured bulk magnetic properties. Furthermore, the
18 serpentized samples show a larger variability in the direction of the magnetization and a stronger heterogeneity
19 with respect to the pristine sample. The ability to rigorously associate components of the bulk magnetic properties
20 to individual mineral phases creates new possibilities for rock magnetic, paleomagnetic, and exploration
21 applications.

1. INTRODUCTION AND GEOLOGICAL SETTING

22 Geological samples have a wide range of magnetic properties depending on quantity of ferromagnetic minerals,
23 and their compositions, grain sizes and microstructures. These properties influence magnetic anomalies from the
24 micro- to the planetary scale. The natural remanent magnetization (NRM) of a sample is additionally dependent
25 on the time and conditions of magnetic acquisition, so it reflects and can record the geological history of the
26 sample. Secondary processes such as serpentinization or metamorphism can significantly alter both mineralogical
27 characteristics and NRM, dramatically affecting rock magnetic properties and in turn changing the nature of the
28 magnetic anomalies. Therefore, a comprehensive characterization of the magnetic petrology of the rock and its
29 thermal history is needed for accurate interpretation of magnetic anomalies.

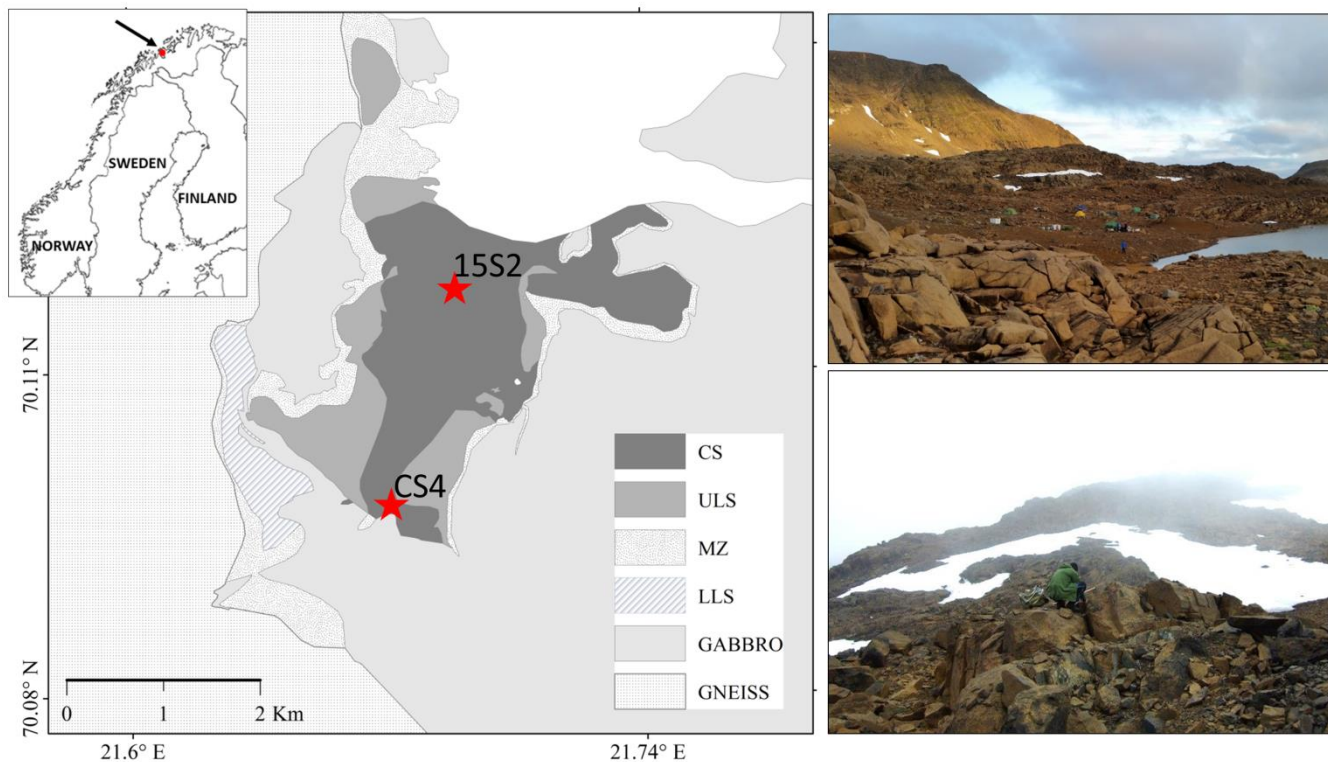
30 Rock magnetic methods are widely applied to measure rocks magnetic properties and characterize the carriers.
31 While indispensable, traditional methods are bulk measurements that do not directly relate magnetic properties to
32 individual mineral phases or microstructures. To attribute specific magnetic signals to the underlying mineralogy,
33 techniques must be employed that can resolve magnetic properties at a fine scale. The ability to discriminate
34 differing behavior of constituent phases is necessary for a complete understanding of the origin of bulk behavior
35 measured in both the laboratory and in magnetic surveys, and provides vital evidence about primary and
36 secondary geological processes and their role in determining magnetic response. One such technique that offers
37 spatially-resolved measurements of magnetic signals is scanning magnetic microscopy (e.g. Fu et al., 2014;
38 Fukuzawa et al., 2017; Hankard et al., 2009; Lima et al., 2014; Noguchi et al., 2017; Oda et al., 2011; Tominaga
39 et al., 2017; Weiss et al., 2000; Weiss et al., 2007). This emerging technique generates an accurate map of the
40 magnetic field distribution over a planar surface of a rock sample with sub-millimeter resolution. Previous
41 applications of scanning magnetic microscopy have been primarily as an extension of, and complement to
42 traditional paleointensity and paleomagnetic techniques. Weiss et al. (2008) used the technique to investigate fine
43 scale heterogeneity of magnetization in Martian meteorites and estimate the ancient Martian field strength.
44 Paleointensity estimates are commonly based on bulk measurements, and do not account for the non-
45 unidirectional orientation of the fine scale magnetization of the sample, which controls the bulk properties.

46 Tominaga et al. (2017) investigated changes in the magnetic field intensity with the mineralogy during a
47 carbonation sequence and used scanning magnetic microscopy to trace the reaction front. Oda et al. (2011) and
48 Noguchi et al. (2017) used SQUID magnetic microscopy to generate a fine scale magnetostratigraphy to estimate
49 ages and growth rate of ferromanganese crust. While scanning magnetic microscopy has been applied in Earth
50 sciences for several decades (Thomas et al., 1992), interpretation of the data remains an unresolved problem. Most
51 previous work modeled the data acquired by scanning magnetic microscopy in terms of dipole moment intensity
52 and directions, which is sufficient for paleomagnetic and paleointensity studies and appropriate for sources with
53 simple geometries. However, laterally extensive sources, or those with non-uniform magnetization, common in
54 nature, may not be accurately de-scribed by single dipole field. Furthermore, comparison with bulk measurements
55 requires that the volume of the magnetic material be taken into account, hence calculating magnetization, rather
56 than moment. Weiss et al. (2002) describe an inversion method to calculate the magnetization distribution from
57 magnetic scan data using a grid of evenly spaced dipoles, with a fixed volume for grid voxels. The size of the data
58 sets, however, means that such methods are computationally intensive and time-consuming. Here, we propose an
59 alternative approach to a full scan inversion, or to the dipole moment determination. This consists of forward
60 modeling of the magnetization of a three-dimensional source geometry using the compositional and geometrical
61 constraints given by optical and electron microscopy. This approach, by including the geometry of the source,
62 limits the degrees of freedom which characterize the inherently non-unique magnetic data inversions. We propose
63 forward modelling to estimate the magnetization of discrete sources. When applied to the entire sample, the
64 magnetization estimates of discrete grains can then be compared to the bulk properties of the sample.

65 Here, scanning magnetic microscopy and forward magnetic modeling are used in combination with chemical and
66 magnetic properties analyses to characterize the magnetic carriers in three samples; a pristine dunite sample
67 (CS4), and two highly serpentinized samples (15S2D and 15S2B).

68 The samples are from the Reinfjord Ultramafic complex (RUC)(Fig. 1), of the Seiland igneous province (SIP) in
69 northern Norway. This complex was emplaced during the Ediacaran at a depth of 25–35 km (Larsen et al., 2018)
70 and later uplifted. The SIP is now exposed in the Middle Allochthon of the Norwegian Caledonian belt. Although
71 the SIP has a complex geodynamic history, most of the magmatic textures of its rocks are well preserved. The

72 samples were selected to examine the origin of the primary magnetization in the dunite, and the effect of later
73 serpentinization on the bulk properties. The pristine samples are believed to preserve primary NRM carriers of the
74 lower crust, a topic of debate that is strongly linked to the thermal history of the rocks (McEnroe et al., 2018). In
75 addition, there are local serpentinized areas within the ultramafic outcrops. Serpentinization is a relatively low
76 temperature (≤ 400 °C) fluid-mediated hydration process and in ultramafic rocks commonly leads to the
77 production of magnetite. The creation of secondary magnetite could result in a composite NRM of the rock, a
78 combination of the primary and secondary magnetizations, or may completely overprint the original NRM. The
79 characterization of the NRM of discrete magnetite grains could be useful to distinguish different stages of
80 serpentinization. By directly relating the micrometer scale anomalies to the mineralogy, we can improve our
81 understanding of processes that control the magnetism of a rock and link these to the geological history. A greater
82 understanding of the processes and features at the mineral scale will enhance our interpretation of magnetic
83 anomalies on outcrop, regional, and planetary scales.



84
85 **Fig. 1. Geological map of the Reinjfjord Ultramafic Complex (modified after Grannes, 2016) with samples**
86 **localities (red stars); CS4 sample is taken from the southern side of the complex, while the 15S2 locality is from**

87 *the northern side. Right: outcrops photographs of the dunite rocks from the Central Series formation. The*
88 *ultramafic complex, surrounded by gabbroic rocks and gneisses, consists of three ultramafic series: the Central*
89 *series (CS), the upper layered series (ULS) and the lower layered series (LLS).*

2. METHODS

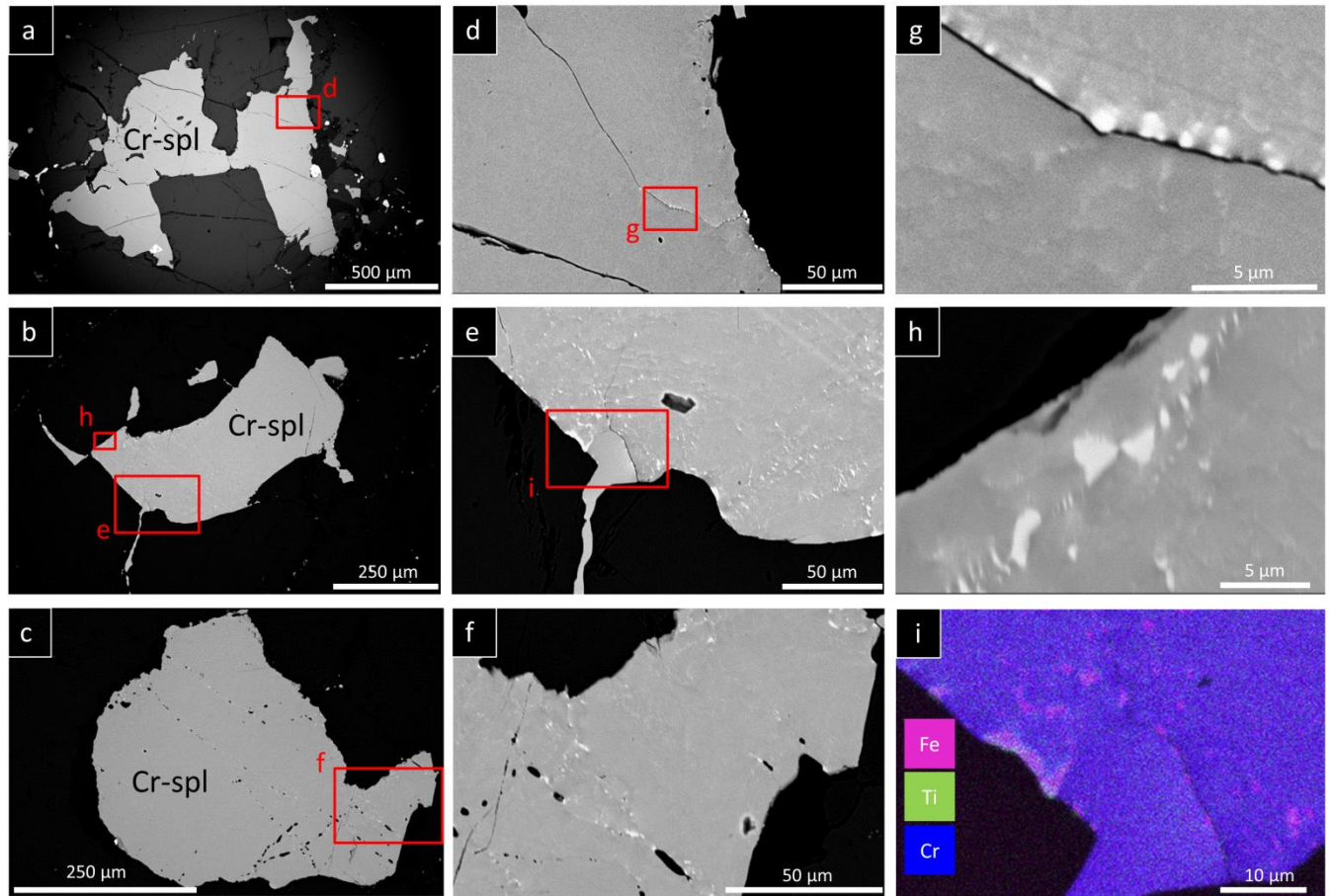
90 We investigated three samples of the Reinfjord Ultramafic Complex with optical and electron microscopy, rock
91 magnetic methods, and magnetic modeling. Microscopy provides precise measurements of size, shape, and
92 chemical composition of oxide and sulphide particles in a thin section, which had been surveyed in the scanning
93 magnetic microscope before exposure to electron microscope fields. Bulk magnetic properties were measured on
94 chips or cores of companion samples. Magnetic modeling of the magnetic microscopy scans of the thin sections
95 was applied to isolated anomalies associated with discrete grains to estimate the magnetization intensity and
96 direction of the magnetic grains. Modal mineralogy was investigated using optical and scanning electron
97 microscopy (SEM) imaging by backscattered electrons at the NTNU NanoLab using a FEI Helios G4 UX
98 scanning electron microscope (SEM). Chemical analyses were made using a JEOL 8200 SuperProbe (Electron
99 Probe Microanalyzer-EPMA) at the University of Milan using wavelength-dispersive spectroscopy (WDS)
100 techniques. All samples were analyzed at the microprobe with a spot current of 5 nA and 15 keV accelerating
101 voltage. Points were spot analyzed with a beam diameter of 1 μm and measuring time of 10 s on background and
102 30 s on peak. Thin-sections magnetic scans were made with a scanning SQUID microscope at the Geological
103 Survey of Japan, National Institute of Advanced Industrial Science and Technology (AIST), and on a newly built
104 scanning magnetic tunnel junction instrument (here after referred to as the MTJ microscope) at the NTNU Rock-
105 and Paleomagnetism laboratory. Both instruments measure the vertical component of the field and all imaging
106 was carried out at room temperature ($\sim 20^\circ\text{C}$) in field-free conditions. Therefore the signals represent remanent
107 behavior. The nominal sampling step for all scans is 100 μm in x and y. The SQUID microscope system uses a 200
108 \times 200 μm square washer type pickup coil, which has a field resolution of 1.1 pT/ $\sqrt{\text{Hz}}$ at 1 Hz (Kawai et al., 2016)
109 and a sample stage with positioning accuracy of $\sim 10 \mu\text{m}$ (Oda et al., 2016). Measurements were conducted with a

110 sensor-to-sample distance of approximately 253 μ m. The MTJ microscope has field noise of ~ 70 nT/ $\sqrt{\text{Hz}}$ at 1 Hz,
111 and positioning accuracy of ~ 100 nm; the poorer noise performance of this instrument is partially offset by aver-
112 aging 5 identical measurements. A sensor-to-sample distance of approximately 200 μ m was used for the surveys
113 with this instrument. The spatial resolution of discrete magnetic sources in both devices is dependent on the
114 sensor active area, scanning step size, positioning accuracy, measurement speed, sensor-to-sample distance and on
115 the thickness of the magnetization distribution. Modeling of the magnetic data acquired by magnetic scanning
116 microscopy was made using Tensor Research ModelVision software. Bulk rock magnetic property analyses were
117 performed at NTNU using a variety of techniques. NRM was measured on sample cores of 2.5 cm diameter and
118 2.2 cm height, or sample chips using an AGICOJR6 spinner magnetometer with sensitivity of 2 μ A/m.
119 Susceptibility values were measured using a Sapphire susceptibility bridge on sample cores and an
120 AGICOMFK1-A Kappabridge on sample chips with sensitivity of 6 $\cdot 10^{-8}$ SI. Temperature dependence of AC
121 susceptibility was measured in argon, and in air using an AGICOMFK1-A-Kappabridge on powdered samples.
122 For high temperature measurements, samples were heated from room temperature (RT) to 700 $^{\circ}\text{C}$ before cooling
123 again to ambient temperature at an interval of 11 $^{\circ}\text{C}/\text{min}$; for low temperature run, samples were cooled from
124 room temperature to -194 $^{\circ}\text{C}$ and then heated back to room temperature. High- and low-field susceptibility,
125 saturation remanence (M_r) and saturation magnetization (M_s) curves were measured as a function of temperature
126 using a Princeton PMC Model 3902/F MicroMag Vibrating Sample Magnetometer (VSM) with a flowing helium
127 furnace instead. The instrument measures the magnetic moment with an average sensitivity of 0.5 nA \cdot m 2 .
128 Measurements were made on chips of the samples using the quarter-hysteresis loop method of Fabian et al. (2013)
129 here with a maximum field of 1 Tesla. Curie temperatures and blocking behavior were estimated from
130 thermomagnetic curves. Room temperature hysteresis measurements were acquired before and after each thermal
131 experiment.

3. DATA AND RESULTS

3.1. PETROGRAPHY AND MINERAL CHEMISTRY

132 The three RUC samples discussed here are a pristine dunite sample CS4, and two serpentinized dunite samples
133 15S2D and 15S2B. Samples contain minor opaque phases including oxides and sulfides (pentlandite, pyrrhotite
134 and chalcopyrite). Accessory amounts of amphibole, pyroxenes, calcite, dolomite and biotite are also present.
135 Based on image analysis of optical images, mineral phases abundances of sample CS4 result is 92.3% olivine in
136 large subhedral crystals (1–3 mm in size), 7% pyroxenes (diopside and enstatite), occurring as interstitial grains
137 between olivine grains, and the remaining 0.7% opaque minerals, including oxides and sulfides. The dominant
138 opaque mineral is Cr-spinel. Minor amounts of ilmenite and pentlandite are present. Opaque grain sizes are ≤ 0.1 –
139 mm. Backscattered electron (BSE) images of the Cr-spinel grains show these are not homogeneous and host fine-
140 grained Fe-rich intergrowths (Fig. 2) with sizes varying from ≤ 200 nm to $5\mu\text{m}$. The Fe-rich exsolution 'blebs' are
141 all designated as ferrichromite; however there is a variation in Fe-rich compositions and some are near or end-
142 member magnetite. In the heavily serpentinized samples (15S2D and 15S2B) olivine has been mostly replaced by
143 lizardite, brucite and magnetite; however, some relict olivine and pyroxene grains are recognizable in cross-
144 polarized light. Based on image analyses of optical images, sulfides and oxides constitute up to the 7% of the
145 serpentinized samples. The sulfides are mostly pentlandite and pyrrhotite with minor chalcopyrite. The main
146 oxides are magnetite, ilmenite and Cr-spinels. Backscattered electron (BSE) images of opaque minerals show that
147 spinel grains from serpentinized samples are homogeneous, unlike the Cr-spinel grains in CS4. Magnetite is
148 present throughout the thin section, in small few-micrometer-thick veins (Fig. 3g, h), or in large grains (up
149 to $700\mu\text{m}$) together with pentlandite (Fig. 3), Al-Cr spinel and ilmenite (Fig. 3a, c, d). Of the opaque grains,
150 ferrichromite, magnetite and monoclinic pyrrhotite retain a remanent magnetization. Because the magnetic
151 properties of these phases are strongly controlled by their composition, precise chemical analyses were measured.
152 Measurements were taken from a homogeneous spot area at the microprobe scale. Analyses were calculated as
153 weight percent of oxides. Representative analyses of spinels are shown in Table 1. Cations ratios are given per
154 formula unit (p.f.u.).



155

156

157

158

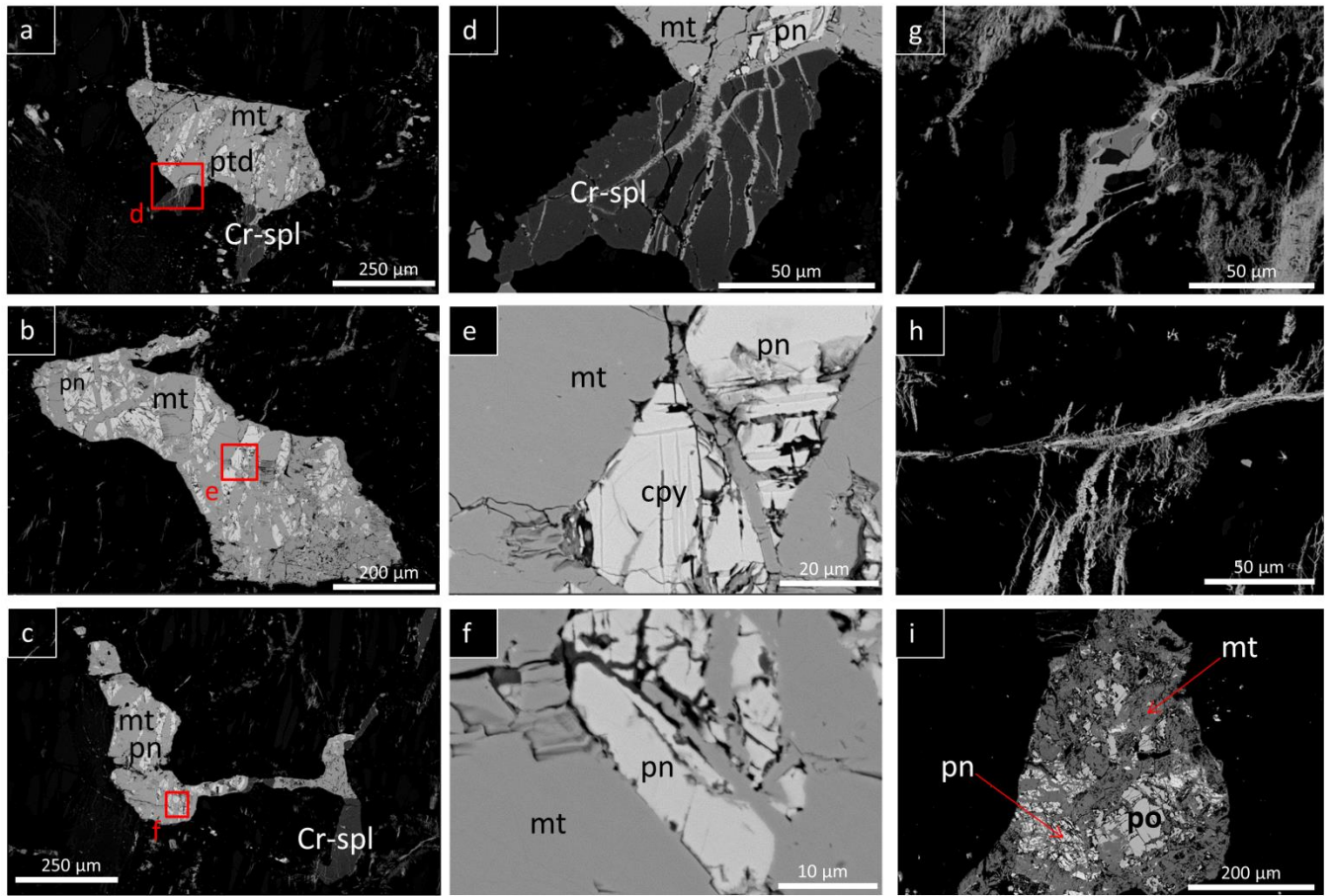
159

160

161

162

Fig. 2. SEM electron backscatter images from sample CS4 (a-h) and element (Fe, Ti, Cr) map from EMP (i). a) Cr-spinel and (d, g) close up images on the same grain. Cr-spinel is in dark gray, and ferrichromite exsolution blebs are light gray. b) Cr-spinel grain and (e, h) close up images on the same grain. Larger ferrichromite intergrowths occur on the margins at the contacts, or along fractures of the hosting grain. c) Cr-spinel grain and (f) close up images on the same grain. i) Elements map for selected area (red box in Fig. 2e) showing ferrichromite (pink) and areas enriched in Ti, enclosed within a matrix of a Cr- and Al rich spinel (blue).



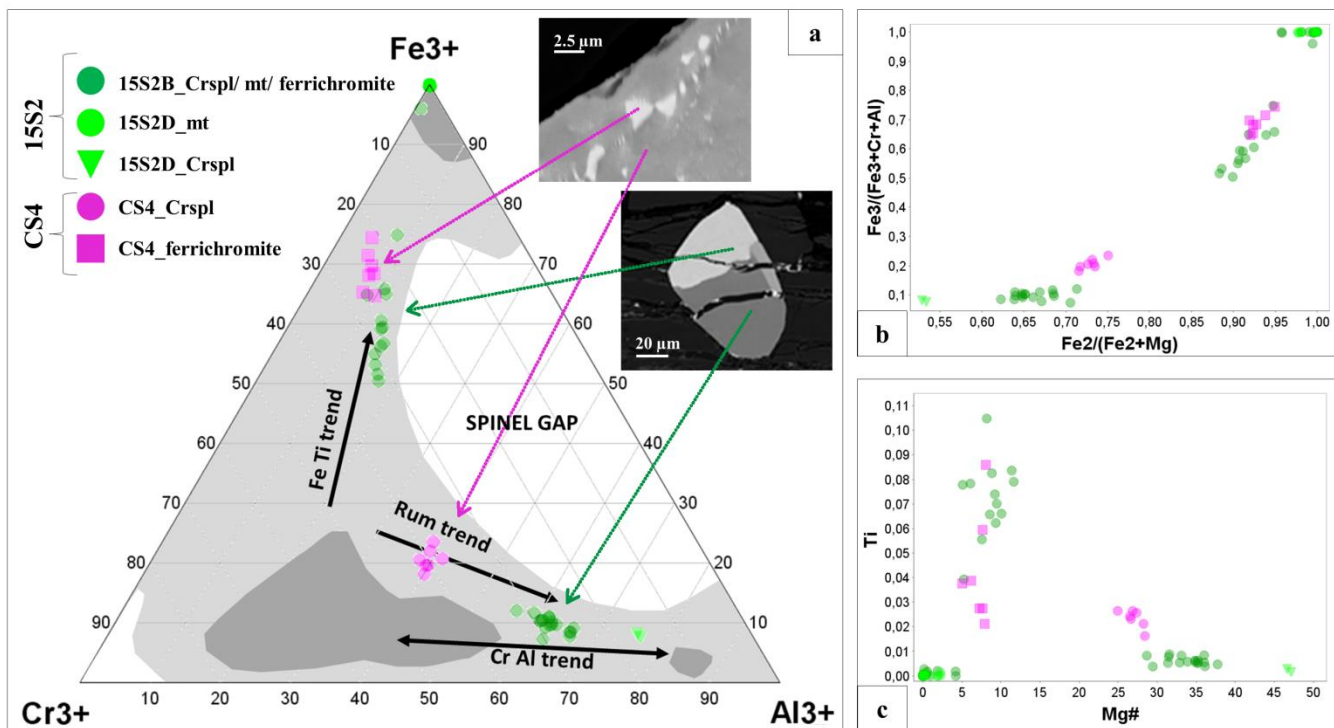
163
 164 *Fig. 3. SEM electron backscatter images from sample 15S2D. a) Magnetite (mt), pentlandite (pn) and Cr-spl*
 165 *assemblage and close up images on the grain (d). b) Magnetite, pentlandite assemblage and close up on the*
 166 *grain (e). c) Magnetite, pentlandite and Cr-spl assemblage and close up on the grain (f). g) Magnetite and*
 167 *Cr-spl in serpentine vein. h) Magnetite in vein. i) Magnetite (dark gray), pentlandite (light gray) and*
 168 *pyrrhotite (po) (medium gray) assemblage.*

169 The larger oxides grains in the pristine dunite sample (CS4) contain two phases (Fig. 2). The host grain consists of
 170 Cr-spinel with modal composition $(\text{Fe}^{2+}_{0.76} \text{Mg}_{0.25})_{1.01} (\text{Fe}^{3+}_{0.46} \text{Cr}_{0.74} \text{Al}_{0.75} \text{Ti}_{0.03})_{1.97} \text{O}_4$, while the exsolved phase
 171 is ferrichromite with modal composition $(\text{Fe}^{2+}_{0.94} \text{Mg}_{0.07} \text{Ni}_{0.01})_{1.02} (\text{Fe}^{3+}_{1.33} \text{Cr}_{0.46} \text{Al}_{0.15} \text{Ti}_{0.03})_{1.97} \text{O}_4$. Magnetite is
 172 the predominant Fe-Ti oxide in the serpentinized samples, and occurs in a wide range of grain sizes, varying from
 173 $< 1 \mu\text{m}$ to $> 400 \mu\text{m}$. Cr-spinel is also present, however, it is more enriched in Al and Mg, and less enriched in Fe
 174 and Cr than in CS4, with modal composition $(\text{Fe}^{2+}_{0.53} \text{Mg}_{0.46})_{0.99} (\text{Fe}^{3+}_{0.15} \text{Cr}_{0.32} \text{Al}_{1.52})_{1.99} \text{O}_4$. The Cr-rich spinel

175 grains in the serpentinized samples do not contain exsolution microstructures observed in the dunite sample, CS4
176 (see Fig. 2).

177 Spinel compositions from the dunite and serpentinite samples are shown on three plots in Fig. 4. In both dunite
178 and serpentinized samples there is a bimodal distribution with a slight shift of the serpentinized samples' spinels
179 (green symbols, Fig. 4a) towards higher Al content with respect to those from CS4 (pink) (Fig. 4a). Ti is present
180 in only small amounts (0.0–0.33 p.f.u.); however spinels with higher Fe³⁺ content or Mg# in the range 5–12 (Fig.
181 4c), have more variable Ti content. A ternary plot of trivalent cations for the samples analyzed is shown
182 in Fig. 4 and data are compared with the mafic and ultramafic spinel compositional fields from Barnes and Roeder
183 (2001). The host and exsolved phases in the pristine dunite sample and the co-existing spinels in the serpentinite
184 samples are separated due to the miscibility gap (“Spinel Gap” in Fig. 4a) in the solid solution. Data from our
185 study plot along the three trends indicated as Cr\Al, Fe\Ti and Rum trends. According to Barnes and Roeder
186 (2001) the Cr\Al trend is the result of equilibria between Al-bearing pyroxenes and Mg-rich spinels. Among the
187 Fe-poor spinel grains, we observe a general enrichment in Al in spinels from the serpentinized sample with
188 respect to those from the pristine dunite. This difference could be related to primary local heterogeneity in the
189 melts, or to reaction of the primitive spinels with the silicates during later serpentinization. The formation of
190 lizardite at the expense of diopside would cause an increased Al/Mg ratio in the fluid. The increased mobility of
191 Fe, generally observed after serpentinization, can further favor iron oxide production and particularly the
192 crystallization of magnetite (top corner in Fig. 4a and top right corner in Fig. 4b), the endpoint of the Fe\Ti trend.
193 Barnes and Roeder (2001) attribute the Fe-Ti trend to either the evolution of spinel compositions during fractional
194 crystallization of silicates with consequent increase of Fe/Mg ratio and Ti content of the melt (Fig. 4c), or to the
195 exchange of Fe²⁺ and Mg between spinel and coexisting silicates. In Fig. 4a spinels from both the dunite and
196 serpentinized samples plot along this trend and show variable Ti contents (Fig. 4c). The ferrichromite exsolution
197 blebs (pink squares), previously shown in Fig. 2 are hosted by the Fe-poor spinels. The CS4 spinels are well
198 grouped and have similar composition with Mg# between 24 and 28. The spinels from the serpentinized sample
199 have a larger Mg# range and slightly lower Ti content. These differences result in an overlap with the Rum trend.
200 This trend describes an increase in Al at the expense of Cr with decreasing Fe³⁺, and has been attributed to the

201 reaction between cumulus spinel grains and intercumulus liquid (Barnes and Roeder, 2001). We do not exclude
 202 that during serpentinization primary spinels have incorporated Al at the expense of Fe^{3+} , which has been
 203 accommodated instead the newly formed iron oxides.



204
 205 *Fig.4. Spinel compositional data for CS4 (pink) and 15S2 (green). a) Ternary plot of trivalent cations (atomic*
 206 *Cr^{3+} , Fe^{3+} , Al^{3+}) with spinels compositional fields (different gray colors on the background are for different*
 207 *data concentrations) and trends (black arrows) from Barnes and Roeder (2001). Illustrative SEM backscatter*
 208 *images for spinels compositions from CS4 and 15S2 samples. (b) $Fe^{2+}/(Fe^{2+} + Mg)$ versus $Fe^{3+}/(Fe^{3+} + Cr + Al)$.*
 209 *d) Ti versus Mg# ($Mg/(Mg + Fe^{2+})$).*

210

211 **Table 1. Representative Wavelength-dispersive (WDS) chemical compositions of spinels in pristine dunite**
 212 **(CS4) and serpentized (15S2D) samples. Values in parentheses correspond to 1 σ standard deviation; n is the**
 213 **number of analyses. Detection limits ranges on analyzed elements are indicated for each group of analyses.**

Sample	CS4				15S2D			
	n = 5		n = 5		n = 6		n = 2	
TiO ₂	0.97	(0.17)	1.81	(0.83)	0.01	(0.01)	0.10	(0.04)
Al ₂ O ₃	20.22	(0.77)	2.79	(0.58)	0.00	(0.01)	45.63	(0.24)
Cr ₂ O ₃	30.13	(1.70)	15.63	(1.43)	0.00	(0.01)	14.51	(0.11)
Fe ₂ O ₃	16.79	(1.42)	48.11	(2.99)	70.25	(0.31)	7.37	(0.44)
FeO	27.39	(0.37)	31.37	(0.26)	31.53	(0.18)	22.38	(0.11)
MnO	0.28	(0.04)	0.21	(0.03)	0.03	(0.03)	0.17	(0.02)
MgO	5.64	(0.29)	1.31	(0.25)	0.02	(0.02)	11.09	(0.11)
NiO	0.08	(0.05)	0.21	(0.05)	0.08	(0.06)	0.23	(0.01)
Total	101.50		101.44		101.94		101.46	
Normalized to 3 Cations and 4 Oxygens								
Ti	0.023	(0.005)	0.050	(0.023)	0.000	(0.000)	0.002	(0.001)
Al	0.778	(0.026)	0.121	(0.025)	0.000	(0.000)	1.516	(0.010)
Cr	0.763	(0.040)	0.452	(0.040)	0.000	(0.000)	0.323	(0.002)
Fe ³⁺	0.412	(0.043)	1.325	(0.080)	1.996	(0.002)	0.156	(0.009)
Fe ²⁺	0.742	(0.016)	0.960	(0.013)	0.996	(0.003)	0.527	(0.003)
Mn	0.008	(0.001)	0.007	(0.001)	0.001	(0.001)	0.004	(0.001)
Mg	0.271	(0.014)	0.072	(0.013)	0.001	(0.001)	0.466	(0.004)
Ni	0.003	(0.001)	0.006	(0.001)	0.003	(0.002)	0.005	(0.000)
Total	3.000		2.993		2.997		2.999	
Detection limits ranges (ppm)								
Ti	310-353		331-367		343-407		291-320	
Al	143-162		141-153		141-155		170-173	
Cr	381-410		380-412		408-423		334-350	
Fe	373-399		413-457		450-468		351-351	
Mn	411-469		392-420		362-403		338-368	
Mg	136-178		132-158		118-153		169-167	
Ni	407-433		424-473		439-468		367-402	

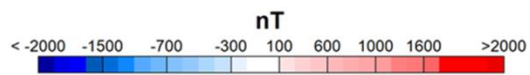
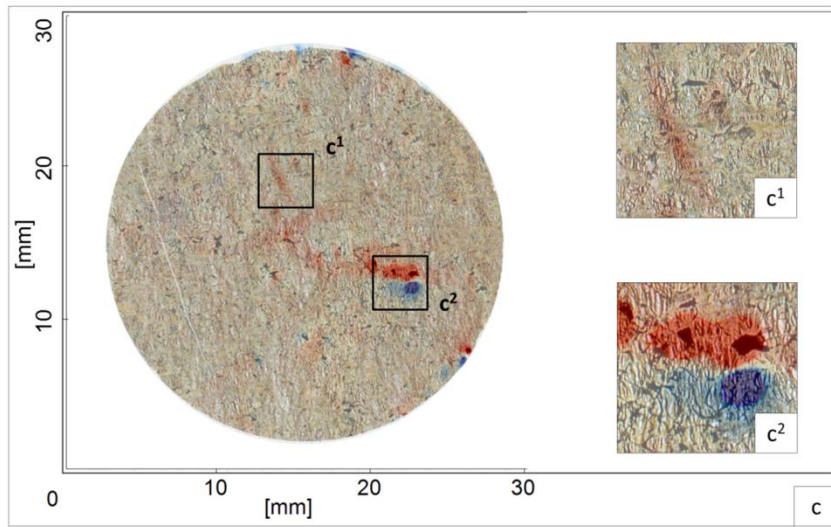
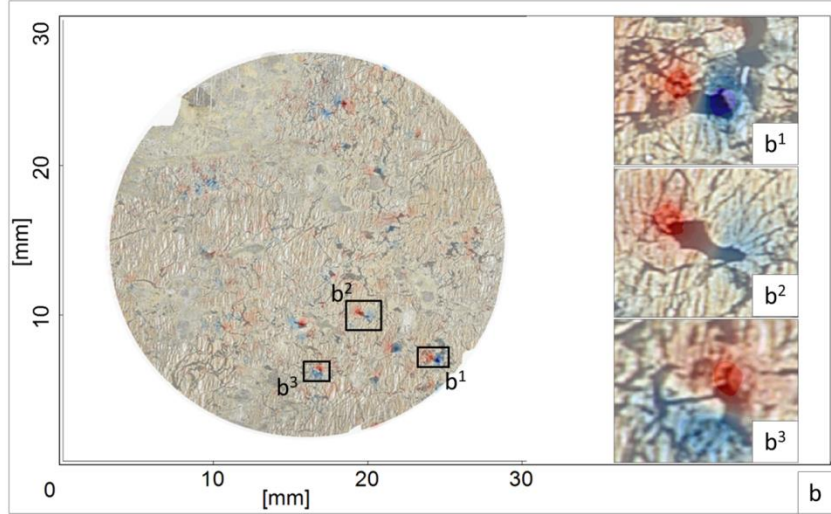
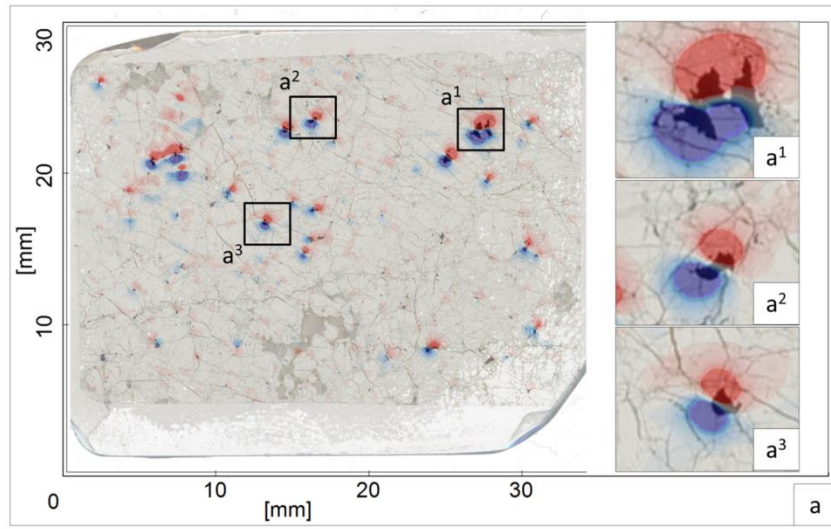
214

3.2. SCANNING MAGNETIC MICROSCOPY

215 The magnetic scans of pristine sample CS4 and serpentized 15S2D were acquired with a scanning SQUID
 216 microscope at the Geological Survey of Japan (GSJ) (Oda et al., 2016). The third scan (15S2B, serpentinite) was

217 made at the NTNU laboratory of rock magnetism and paleomagnetism using a scanning magnetic microscope
218 equipped with a magnetic tunnel junction sensor (Church and McEnroe, 2018). The thickness of the thin sections
219 is 30 μ m.

220 Aligned overlays of optical and magnetic scans of the thin sections are shown in Fig. 5. All scans measure the
221 vertical component of the magnetic field and are shown on the same color scale. The measured field intensity
222 ranges from -7500 nT to +8100 nT for CS4, from -2200 nT to +2300 nT for 15S2D and from -5000 to +9900 nT
223 for 15S2B. In each scan several isolated magnetic anomalies related to discrete opaque mineralogy are observed.
224 In the dunite sample (CS4) the anomalies are commonly dipolar, in the plane of the sample, and oriented NE-SW
225 (Fig. 5a). Slight variations in the directions are likely related to the shape and orientation of the grain. Most of the
226 anomalies correlate with grains with an average surface of 300 μ m*300 μ m. With thin section thicknesses of
227 30 μ m, this results in a high aspect ratio of the grains (\approx 10) which could influence the direction of magnetization.
228 In 15S2D the anomalies are dipolar and in the plane of the sample, but are more randomly oriented compared to
229 those in CS4. The amplitude of the anomalies is comparable, or lower than those observed in CS4. The 15S2B
230 scan is dominated by three high-intensity anomalies that correlate with large (> 200 μ m diameter) grains of
231 magnetite with pentlandite and chalcopyrite, two at the edge of the sample and one in the SE quadrant (Fig. 5c).
232 Weaker and elongated anomalies are also present and correlate with the diffuse, fine magnetite in the
233 serpentized veins. The anomalies in the 15S2B thin section fall into two similar groups. The rounded, high
234 intensity, in-plane signals are correlated with larger opaque grains and are similar to the stronger anomalies
235 observed in 15S2D. The weaker, elongated anomalies correlate with the fine magnetite in serpentine veins. The
236 two types of anomalies have two different directions, approximately 90° from each other (Fig. 5c) with the
237 magnetite in the serpentine veins producing a signal approximately normal to the plane of the sample.



239 *Fig. 5. Overlays of the magnetic anomaly maps with the optical scans for (a) CS4, (b)15S2D and (c)15S2B.*
240 *Shown in insets to the right are enlarged views of selected anomalies. Figs. 2 and 3 show high-magnification*
241 *SEM backscatter images of the same opaque grains causing the anomalies in a^1 , a^2 , a^3 (CS4) and b^1 , b^2 , b^3*
242 *(15S2D) respectively. All magnetic scans measure the vertical field and are displayed with the same color scale*
243 *in nT*

3.3. ROCKS MAGNETIC AND PHYSICAL PROPERTIES

244 The concentration, composition, grain size, shape, and inter-growths or microstructures of magnetic minerals
245 strongly control rock magnetic properties and particularly their ability to retain a stable magnetic memory over a
246 geological time span (McEnroe et al., 2009a, 2009b; Robinson et al., 2016). Magnetically-ordered phases that
247 possess spontaneous magnetization and are able to carry remanent magnetization are iron nickel alloys,
248 uncommon in crustal rocks, or iron oxides and iron sulfides (monoclinic pyrrhotite). For the iron oxides in the
249 chromite-magnetite solid solution the balance between Fe and Cr (or other cations) controls the magnetism of and
250 affects intrinsic properties such as the Curie temperature (Robbins et al., 1971). Increasing substitution of cations
251 such as Ti, Cr, Al and V in magnetite at the expense of Fe lowers the Curie temperature, although in whole-rock
252 samples minor substitution does not necessarily produce weaker magnetic low-field susceptibility, or
253 thermoremanent magnetization intensity, which in turn are more affected by grain size than composition (Clark,
254 1997). Here we investigated magnetic properties of the samples and estimate the Curie temperature,
255 concentration, and grain size of the magnetic carriers using established magnetic methods, described below.

3.3.1 NATURAL REMANENT MAGNETIZATION, MAGNETIC SUSCEPTIBILITY AND DENSITY

256 The samples show distinctly different bulk magnetic and density properties, due to the effect of serpentinization
257 on diverse petrophysical parameters (Table 2). The NRM varies between 0.6 and 1.0 A/m in the pristine sample
258 and between 2.7 and 6.9 A/m in the serpentinite. The magnetic susceptibilities of the serpentinite samples are 1-2
259 orders of magnitude higher than the dunite, consistent with the production of magnetite during serpentinization.
260 Densities are significantly lower in the 15S2D and 15S2B cores (average density of 2.8 g/cm^3) with respect to the

261 CS4 core (3.4 g/cm³). Most of the primary olivine and pyroxenes in the serpentinized samples have been replaced
 262 by lizardite or brucite, which have a lower density.

3.3.2 HYSTERESIS PARAMETERS

263 Room temperature hysteresis behavior is primarily controlled by the magnetic mineralogy and the domain state.
 264 The characteristic quantities calculated from the hysteresis loop are saturation magnetization Ms, the remanent
 265 magnetization Mr, and the coercivity field Hc; the coercivity of remanence Hcr is measured using a separate
 266 remanence analysis. Table 2 summarizes hysteresis parameters for the samples, companion specimens were used
 267 for the high-temperature measurements and their properties are summarized in Table A1.

268 *Table 2. Samples densities and magnetic properties (left side of the table), and hysteresis measurements on*
 269 *chips of the samples (right side of the table). Volume percent magnetite is calculated by dividing the magnetic*
 270 *susceptibility (k) by 0.0347 (Clark, 1997) and is calculated from saturation moment by dividing the Ms of the*
 271 *sample by the product of Ms of pure magnetite (480,000 A/m), sample mass and sample density. The*
 272 *Königsberger ratio (Q) is the ratio between NRM and induced magnetization which is calculated multiplying*
 273 *the susceptibility and the local magnetic field (43.0012 A/m). The precision used in the table is significant.*

SAMPLE		Density [g/cm ³]	Susceptibility [SI]	NRM [A/m]	Q	Volume % magnetite from susceptibility	Chip Mass [g]	Mr [Am ² /kg]	NRM/Mr [%]	Ms [Am ² /kg]	Hc	Hcr	Mr/Ms	Hcr/Hc	Volume % magnetite from Ms
CS4	C1 Chip	3.3	0.006	0.7	2.6	0.2	2.73	0.03	0.75	0.12	16.3	37.4	0.22	2.30	0.1
	C2 Chip	3.4	0.006	0.8	3.0	0.2	0.98	0.03	0.89	0.14	13.9	35.9	0.18	2.58	0.1
	C3 Chip	3.3	0.007	1.0	3.1	0.2	0.40	0.03	0.90	0.16	13.5	35.0	0.20	2.60	0.1
	CS4 Core	3.4	0.005	0.6	3.1	0.1									
15S2	D1 Chip	2.8	0.089	5.4	1.4	2.6	0.53	2.01	0.10	4.89	30.2	41.7	0.41	1.38	2.8
	D2 Chip	2.6	0.101	5.0	1.2	2.9	0.82	2.14	0.09	5.55	29.7	41.5	0.39	1.40	3.0
	D3 Chip	2.7	0.085	4.7	1.3	2.5	0.86	1.58	0.11	4.40	31.2	45.7	0.36	1.47	2.5
	D Core	2.8	0.048	4.8	2.3	1.4									
	B1 Chip	2.5	0.083	5.9	1.7	2.4	1.31	5.07	0.05	12.68	29.4	41.9	0.40	1.42	2.7
	B2 Chip	2.6	0.067	2.7	0.9	1.9	0.37	1.56	0.06	5.44	27.3	38.0	0.29	1.39	3.0
	B Core	2.8	0.049	6.9	3.2	1.4									

274

275

276 Ms is directly proportional to the magnetic content of the samples and is used to determine the volume magnetite
277 content in the samples. This is estimated to be 2.5–3.0% in the serpentinized samples and 0.1% in the dunite. For
278 the latter, 0.1% is a minimum estimate of the actual volume of ferromagnetic minerals within the sample, because
279 the Ms of magnetite used in the calculation is higher than the Ms of cation-substituted compositions, in the
280 magnetite-chromite solid solution. Therefore there could be slightly higher modal amount of ferromagnetic
281 minerals. The electron microprobe analyses did not reveal endmember magnetite but rather ferrichromite with
282 composition $x=1.4$ in the system $\text{Fe}^{2+}\text{Cr}_{2-x}\text{Fe}^{3+}_x\text{O}_4$. Using this composition and corresponding Ms of 230,000 A/m
283 (calculated from Robbins et al., 1971), the volume percent of magnetic oxides is approximately 0.2 %, double that
284 obtained considering Ms of endmember magnetite. The volume percentage of magnetite can alternatively be
285 calculated as a function of low-field susceptibility, volume % Mgt = volume susceptibility (k)/0.00347, an
286 empirical estimation (Clark, 1997; Puranen, 1989). Estimates of magnetite content using this method included in
287 Table 2 are similar to those calculated from Ms. The susceptibility calculation yields lower estimates for the whole
288 serpentinite cores, which are approximately 30× the size of the individual chip samples. The magnetite estimates
289 from both methods (0.1–0.2% for dunite CS4, 2.4–3.0% for serpentinites 15S2D and 15S2B) have similar trends
290 to the estimate made by image analysis of 0.7% opaque minerals in the dunite and 7.0% in the serpentinite.
291 Because the image analysis measures all opaque grains, including those non-magnetic, it is expected to yield a
292 higher estimate than the magnetic measurements, however on both cases the ratio between the dunite and
293 serpentinite is approximately 10×.

3.3.3 THERMOMAGNETIC BEHAVIOR

294 The Curie point (T_c), is the temperature below which a magnetic ordering generates a net (spontaneous)
295 magnetization and is a diagnostic tool for identification of magnetic minerals. Above this temperature the material
296 is purely paramagnetic (Dunlop and Ozdemir, 1997). End-member magnetite is a commonly occurring natural
297 magnetic oxide and has a distinct Curie point at 580 °C. However within solid solution series, the Curie point
298 temperature varies over a wide temperature range and can be used to constrain the mineral composition, or

299 oxidation state (Fabian et al., 2013; Kądziałko-Hofmökł et al., 2008; Petersen and Bleil, 1982; Readman and
300 O'Reilly, 1972). To measure the Curie temperature, samples are heated in a magnetic field and their susceptibility,
301 or M_s is measured as a function of temperature. Below are the results of the thermomagnetic experiments.

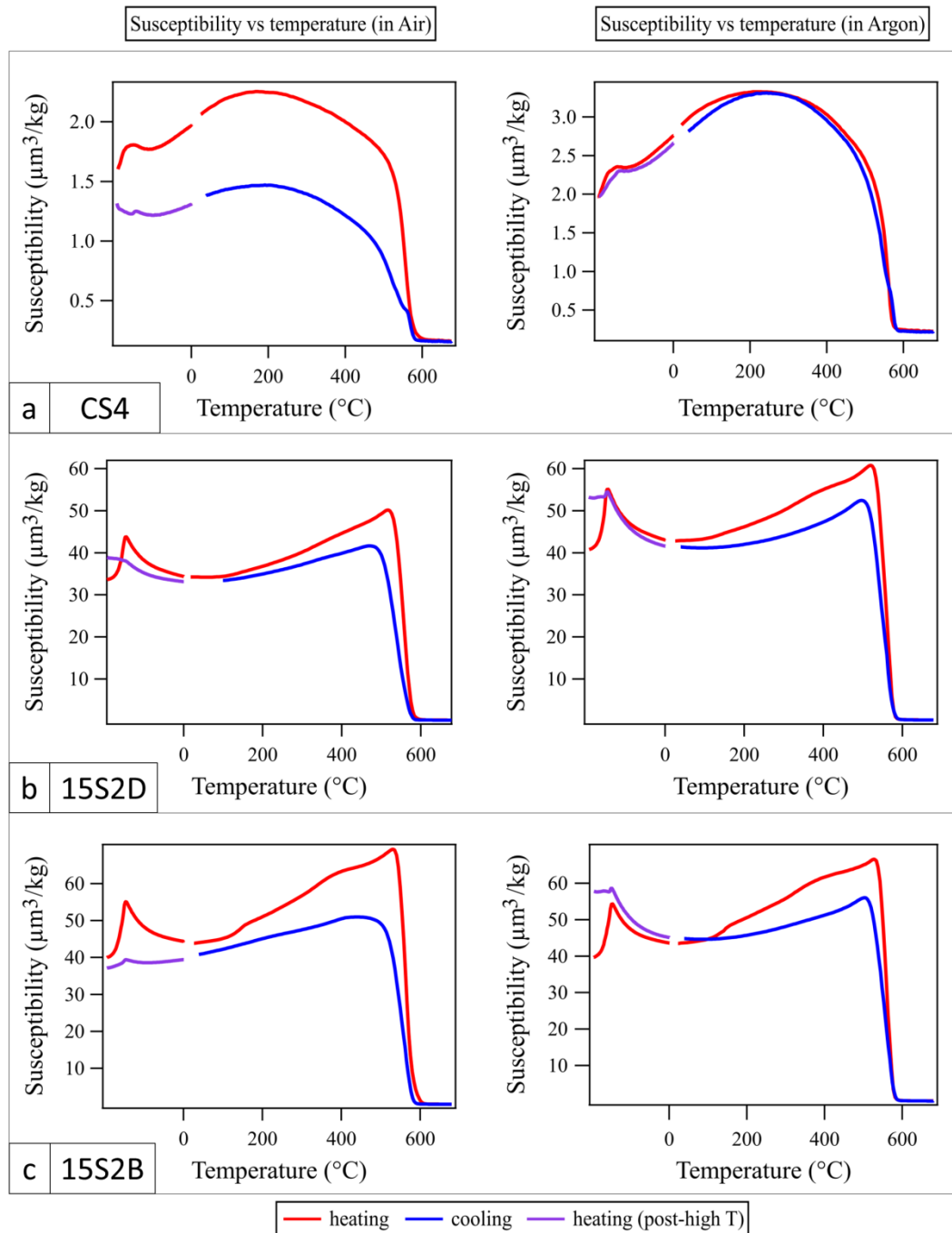
302

3.3.3.1 *LOW FIELD SUSCEPTIBILITY*

303 Sample chips of CS4 and 15S2 were powdered for high-temperature susceptibility measurements. Companion
304 specimens were measured in air and argon, to check for reduction or oxidation during the heating processes on
305 specimens (Fig. 6). Each plot shows a curve for heating and cooling. Low temperature measurements were made
306 before and after heating the sample to high temperature as a further check for alteration that may have occurred.
307 With the exception of the CS4 sample measurement in air (Fig. 6a, left), all other plots show that the susceptibility
308 at room temperature is similar before and after heating. However, in both argon and air measurements, the
309 comparison between the cooling and the heating curves suggests an alteration of the sample with a loss in
310 susceptibility after the heating process. Serpentinized samples show well-defined Hopkinson peak both on heating
311 and cooling at ~ 570 °C, near the Curie temperature of endmember magnetite. This peak, typical of magnetite and
312 other magnetic materials, manifests as an increase in magnetic susceptibility between the blocking and the Curie
313 temperatures and is often indicative of fine-grained particles. The heating branches show a “hump” centered at
314 370 °C in both specimens (Fig. 6b,c) suggesting ferrichromite (Table3). The lower temperature hump between 150
315 and 170 °C may be due to the λ -transition from antiferro- to a ferrimagnetic behavior in pyrrhotite (Minyuk et al.,
316 2013). From optical and electron microscopy pyrrhotite is more abundant in the 15S2B sample with respect to
317 15S2D, consistent with the more pronounced excursions around 150°C in the latter sample. Horen et al. (2014)
318 describe a similar hump as consequence of oxidation and destabilization of ferrichromite with a mechanism of
319 dynamic segregation (Domenichini et al., 2002). This mechanism describes the formation of a new low-
320 temperature magnetic phase and destruction/rehomogenization of the material within the same heating cycle. This
321 rehomogenization would explain the irreversibility of the thermomagnetic curve that shows only magnetite in the

322 cooling curve (Fig. 6b, c). Dehydration and/or reduction of hydroxides may also cause variations in the
323 susceptibility (Funaki et al., 2000) and the irreversibility of the chemical reaction is consistent with the absence of
324 these variations after heating. The dunite sample (CS4) shows smooth heating and cooling curves, concave down,
325 with no Hopkinson peak. The maximum susceptibility is reached around 240 °C for runs carried out in argon, and
326 190 °C for those in air. While the steepest descent in both measurements occurs at 560 °C, indicating abundant,
327 impure but near-endmember magnetite, the steady decline in susceptibility from ~240 °C is interpreted as a wide
328 range of Curie temperatures, and hence, compositional variations. The heating and cooling curves are reversible
329 when measured in argon atmosphere, indicating little change in the magnetic mineralogy during heating.
330 However, there is clear evidence for mineralogical change during the run in air, as indicated by the irreversibility
331 of the thermomagnetic curves (Fig. 6a). On the cooling run, this sample exhibits a small inflection near 520 °C,
332 below the highest Curie temperature. This second Curie temperature suggests a new phase was created during the
333 experiment, possibly due to cation diffusion between the Fe-poor and Fe-rich regions of the Cr-spinel or the onset
334 of spinodal decomposition. All samples exhibit the Verwey transition, an abrupt excursion in magnetic
335 susceptibility near -153 °C (120 K, Walz, 2002, and references therein), which is diagnostic of endmember
336 magnetite. The transition in the pristine dunite is less sharp and begins at a lower temperature than the literature
337 value, suggesting that magnetite has some small degree of cation substitution or non-stoichiometry. By contrast,
338 the Verwey transition in the serpentinite samples (measured before heating) is sharp, indicating a near-
339 endmember composition. Curie temperature estimates (T_c), based on representative composition of the magnetic
340 mineralogy estimated from EMP data and on temperature dependent susceptibility curves, are listed in Tables 3
341 and 4, respectively. For the T_c estimates based on composition data we considered magnetite-spinel $(Fe_3O_4)_x$
342 $(MgAl_2O_4)_{1-x}$ with $0 \leq x \leq 1$ and magnetite-chromite $Fe_{3-x}Cr_xO_4$ $0 \leq x \leq 2$ solid solution series (Table 3). For the
343 magnetite-spinel solid solution series we refer to Harrison and Putnis (1996) where the T_c varies as a function of
344 the mole fraction of magnetite (x) approximated by: T_c (°C) = $-853 + 2410x - 970x^2$. For the magnetite-chromite
345 solid solution series we refer to the combined data sets of Francombe (1957) and Robbins et al. (1971) fit with a
346 logistic function. For comparison T_c estimates based on an interpolation between the two solid solution series are
347 listed in Table 3. In both dunite and serpentinitized samples the Fe-poor spinel compositions are para-magnetic at

348 room temperature. Tc estimates for the ferrichromite vary between 200 °C and 400 °C depending on the cation
349 ratios. To estimate Tc from the initial susceptibility, we used a derivative method that uses the maximum negative
350 slope in the thermomagnetic curve (Table 4).For the serpentinized samples these Tc estimates on the heating
351 curves are in the temperature range of 557–565 °C, whereas the cooling curves show Tc estimates in the range
352 520 °C–572 °C. This variability may indicate that some non-stoichiometric, non-endmember magnetite is present
353 and that paramagnetic elements such as Al, Ti, Cr and/or Mg are substituted in the crystal lattice (Dunlop and
354 Özdemir, 1997), to a greater extent in the dunite than in the serpentinite.



355

356 *Fig. 6. Temperature dependent susceptibility curves in air (to the left) and argon (to the right) for CS4*

357 *(a), 15S2D (b), and 15S2B (c) samples chips. Susceptibility is normalized by the mass of the specimen.*

358

359 *Table . Tc estimates from representative oxides compositions, determined considering magnetite-spinel*
360 *(M-S) (Harrison and Putnis, 1996), magnetite-chromite (M-C) (Francombe, 1957; Robbins et al., 1971)*
361 *solid solution series and an interpolation between the two solid solution series. Chemical formulas do not*
362 *account for elements with 0.01 p.f.u. Pm in the table indicates that the corresponding composition is*
363 *paramagnetic at all temperatures.*

Sample	Spinel Composition	Tc (°C) from composition		
		(Francombe 1957; Robbins et al. (1971))	(Harrison & Putnis 1996)	(considering a combination of the M-C and M-S solid solutions)
CS4	$(\text{Fe}^{2+}_{0.76} \text{Mg}_{0.25})_{1.01} (\text{Fe}^{3+}_{0.46} \text{Cr}_{0.74} \text{Al}_{0.75} \text{Ti}_{0.03})_{1.97} \text{O}_4$ SPINEL/HERCYNITE	-120	-33	-90
	$(\text{Fe}^{2+}_{0.94} \text{Mg}_{0.07} \text{Ni}_{0.01})_{1.02} (\text{Fe}^{3+}_{1.33} \text{Cr}_{0.46} \text{Al}_{0.15} \text{Ti}_{0.03})_{1.97} \text{O}_4$ FERRICHROMITE	400	417	345
15S2D	$(\text{Fe}^{2+}_{0.53} \text{Mg}_{0.46})_{0.99} (\text{Fe}^{3+}_{0.15} \text{Cr}_{0.32} \text{Al}_{1.52})_{1.99} \text{O}_4$ SPINEL/HERCYNITE	-180	<i>pm</i>	-180
	$(\text{Fe}^{2+}_{0.98} \text{Fe}^{3+}_2)_{2.98} \text{O}_4$ MAGNETITE (LARGE GRAINS)	585	586	580
	$(\text{Fe}^{2+}_1 \text{Mg}_{0.02})_{1.02} (\text{Fe}^{3+}_{1.92})_{1.92} \text{O}_4$ MAGNETITE (VEIN)	580	583	580
15S2B	$(\text{Fe}^{2+}_{0.71} \text{Mg}_{0.29})_{1.00} (\text{Fe}^{3+}_{0.24} \text{Cr}_{0.62} \text{Al}_{1.11})_{1.97} \text{O}_4$ SPINEL/HERCYNITE	-150	-185	-125
	$(\text{Fe}^{2+}_{0.93} \text{Mg}_{0.12})_{1.05} (\text{Fe}^{3+}_{0.94} \text{Cr}_{0.57} \text{Al}_{0.30} \text{Ti}_{0.08} \text{V}_{0.02} \text{Mn}_{0.01})_{1.92} \text{O}_4$ FERRICHROMITE	205	276	196
	$(\text{Fe}^{2+}_{0.97} \text{Mg}_{0.05})_{1.02} (\text{Fe}^{3+}_{1.42} \text{Cr}_{0.33} \text{Al}_{0.15} \text{Ti}_{0.04} \text{V}_{0.01})_{1.92} \text{O}_4$ FERRICHROMITE	440	455	414
	$(\text{Fe}^{2+}_{0.99} \text{Fe}^{3+}_{1.98})_{2.97} \text{O}_4$ MAGNETITE	585	585	580
	$(\text{Fe}^{2+}_1 \text{Fe}^{3+}_2)_3 \text{O}_4$ MAGNETITE (LARGE GRAINS)	585	586	580

364

365

366

367 *Table 4. Tc estimates from thermal experiments. Tc estimates based on high temperature measurements*
 368 *are determined from susceptibility (k) and Ms versus temperature curves using the derivative method*
 369 *described in the text. Blocking temperatures (Tb) are derived from Mr. Some samples have multiple Tc*
 370 *estimates in the cooling curve, which reflect the inception of spinodal decomposition during the*
 371 *experiment.*

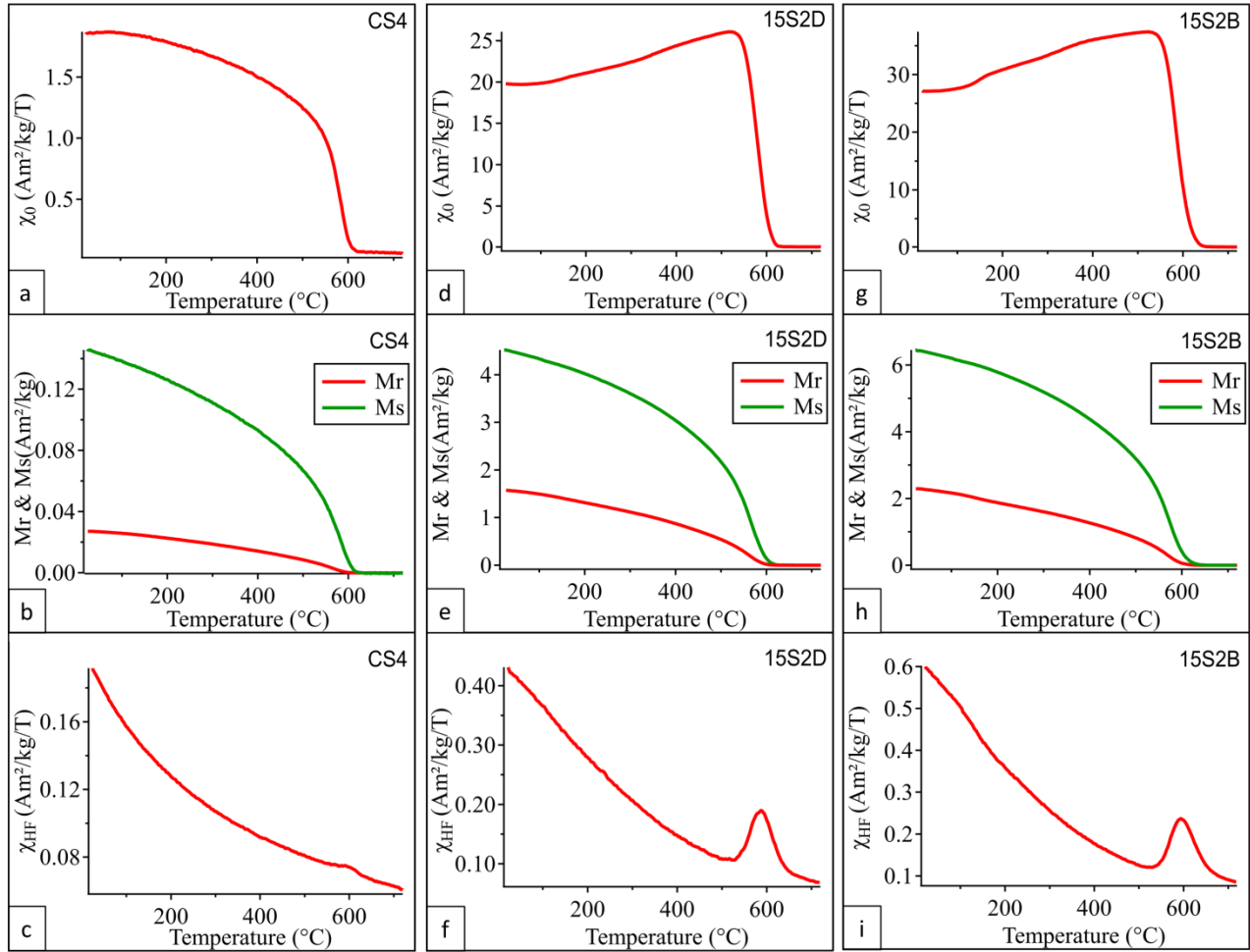
Sample	High-T experiment	Tc (°C) from k		Tc (°C) _Ms	Tb (°C) _Mr
		Heating	Cooling		
CS4	KB air	556	520 568		
	KB Ar	560	545 572		
	VSM	579		576	560
		574			
15S2D	KB air	557	541		
	KB Ar	559	542 561		
	VSM			567	150 561
				565	156 555
15S2B	KB air	565	562		
	KB Ar	148 561	544		
	VSM			576	153 567

372
373

3.3.3.2 HIGH TEMPERATURE VSM MEASUREMENTS

374 An alternative calculation of the Curie temperature and a method to observe the evolution of other informative
 375 metrics as a function of temperature is provided by high-temperature VSM measurements. The advantage of the

376 VSM is that one measures four parameters (M_s , M_r and low- and high-field susceptibility). In strong-field
377 measurements, the variation of the saturation magnetization with temperature is rigorous and more accurate
378 indicator for the Curie temperatures than initial susceptibility and for the identification of ferro-, ferri- and
379 antiferromagnetic states (Fabian et al., 2013; McEnroe et al., 2016). High-temperature curves of M_s , M_r , high-
380 field (χ_{HF}), and low-field (χ_0) susceptibility are shown in Fig. 7 for samples CS4 (a-c), 15S2D(d-f) and 15S2B (g-
381 i) chips. Temperature-dependent initial susceptibility (Fig. 7a, d and g) curves are comparable to those measured
382 on the Kappabridge (Fig. 6), albeit measured with different protocols. Sample CS4 shows a gradual decrease in
383 initial susceptibility followed by a rapid decrease in the temperature range 560–580 °C. By contrast the
384 serpentinized samples (15S2D and 15S2B) show an initial increase in susceptibility followed by a rapid decrease
385 close to the T_c of magnetite. The thermal curves of M_r and M_s are similar in both the 15S2D and 15S2B samples;
386 M_s and M_r slowly decrease with temperature up to 530°C and at a faster rate above this temperature. The point of
387 maximum descent in M_s is a widely-applied technique for estimating the Curie temperature (Tauxe, 1998),
388 though yields a slight underestimation (Fabian et al., 2013), and can be compared to similar calculations from
389 low-field susceptibility measurements in the Kappabridge. T_c estimates based on M_s and unblocking temperatures
390 from M_r are summarized in Table 4. In all samples, the T_c estimated from M_s is higher than that estimated from
391 Kappabridge measurements, to a small degree in sample 15S2D and to a larger extent in CS4 and 15S2B. The M_r
392 curves provide unblocking temperatures, the temperature above which particles have a spontaneous magnetization
393 but due to thermal activation at high temperatures do not carry a stable remanence. The serpentinized samples
394 demonstrate weak unblocking behaviour (with consequent loss of remanent magnetization) near 150 °C. At this
395 temperature there is also a weak enhancement in susceptibility measured in both Kappabridge (Fig. 6) and VSM
396 (Fig. 7) in sample 15S2B. The high-field (HF) susceptibility curve for 15S2 samples shows a clear Landau peak,
397 slightly above Curie temperature for magnetite indicating ferrimagnetic ordering. These temperatures of 588 °C
398 for sample 15S2D, and 595 °C for sample 15S2B, are higher than determinations from M_s , M_r or initial
399 susceptibility, in agreement with Landau theory (Fabian et al., 2013). The Landau peak is visible, though small in
400 the CS4 high-field susceptibility curve.



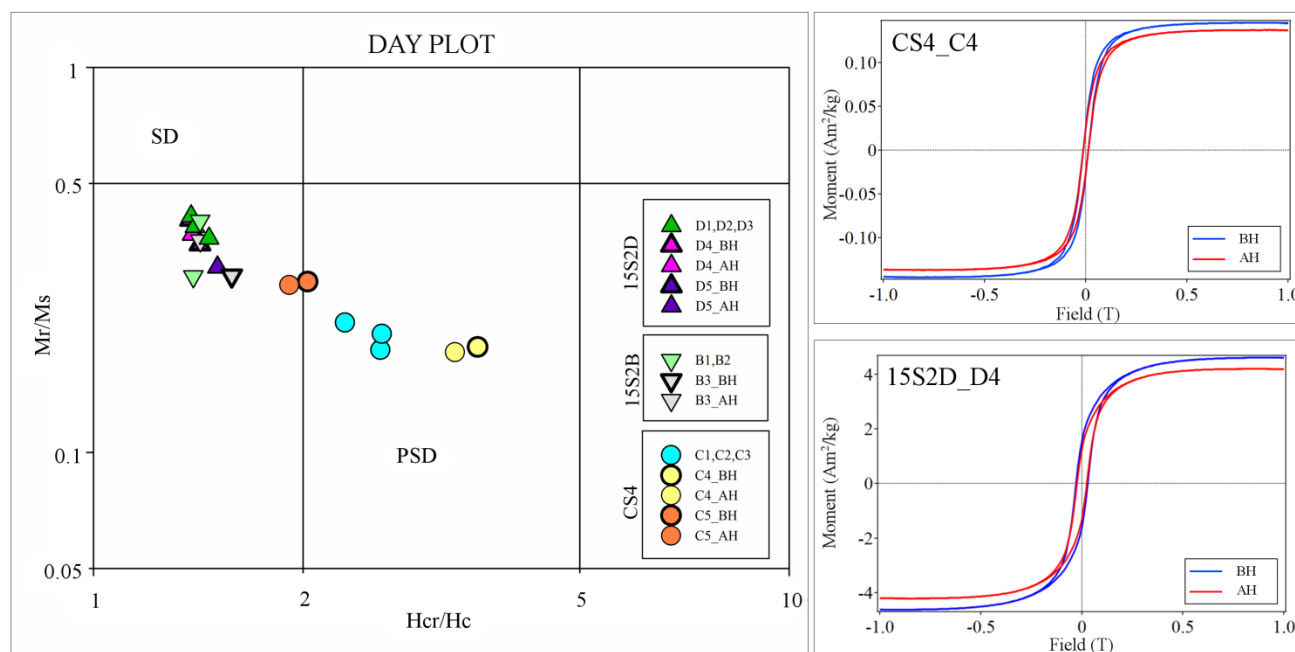
401

402 **Fig. 7. High temperature experiments on 15S2 (15S2D and 15S2B) and CS4 samples chips. (a, d, g) Low-field**
 403 **susceptibility (χ_0) versus temperature. (b, e, h)Mr and Ms versus temperature. (c, f, i)High-field susceptibility**
 404 **(χ_{HF}) versus temperature.**

405

406 Room temperature hysteresis measurements were acquired before and after each thermal experiment, to
 407 characterize the sample, and to check for alteration that may have occurred during the heating. Representative
 408 hysteresis loops, measured before and after the high-temperature VSM experiment are shown in Fig. 8. Hysteresis
 409 loops have been corrected for the paramagnetic contribution to isolate the ferromagnetic response. Both loops
 410 show a decrease in Ms after the high-temperature measurement, indicating some limited mineralogical change.
 411 Comparing the loops before heating, serpentinite sample 15S2D has a wider hysteresis loop than that of the

412 pristine dunite CS4. The wider loop indicates a higher coercivity (H_c) in the serpentinized samples likely related to
 413 the presence of fine-grained magnetite, such as that observed in the veins. Magnetic behavior, particularly
 414 remanence, is strongly influenced by magnetic domain state, which for magnetite can be estimated on the Day
 415 plot (Day et al., 1977). The M_r/M_s and H_{cr}/H_c ratios before and after heating are shown in Fig. 8, with additional
 416 measurements of other chips not used for thermomagnetic measurements, and limits of single-domain and
 417 pseudo-single domain behavior calculated by Dunlop (2002). The serpentinized samples cluster at high M_r/M_s
 418 and low H_{cr}/H_c values, approaching ideal single-domain behavior. By contrast, the pristine CS4 samples lie
 419 outside this cluster with parameters that generally fall within the pseudo-single domain region, which implies that
 420 at least some magnetic particles that contribute to the bulk properties are larger than single-domain. After the high
 421 temperature experiments the values of M_s , M_r , H_c and H_{cr} decrease slightly, indicating a change in chemical
 422 composition, grain size, and/or shape. This change is visible in the hysteresis loops and leads to slight shifts in the
 423 before-(BH) and after-heating (AH) positions of samples on the Day plot.



424
 425 **Fig. 8. Left: Day plot of M_r/M_s versus H_{cr}/H_c for specimens from the serpentinized samples (15S2D and**
 426 **15S2B) and the pristine dunite sample (CS4) (after Day et al., 1977; Dunlop, 2002). CS4 sample plots in the**
 427 **pseudo-single domain (PSD) region while 15S2 samples plot closer to the single-domain (SD) region. These**

428 *parameters are listed in Table 2 and Table A1. BH is before and AH after heating. Right: BH (blue) and AH*
429 *(red) hysteresis loops for CS4_C4 (top) and 15S2D_D4 (bottom).*

3.4. MAGNETIC DATA MODELING

430 Scanning magnetic microscopy provides high resolution mapping of magnetic fields above the thin sections. The
431 technique measures the vertical component of the magnetic field in field-free condition originating from the
432 sample NRM. The measurements, made at room temperature can be correlated with the bulk magnetic properties
433 of the sample. The magnetic field varies across the study thin sections, and is used to locate the magnetic carriers.
434 These were investigated in both magnetic properties and mineral chemistry. The pristine dunite sample has
435 distinctly different NRM intensity and susceptibility values than the serpentized samples (Table 2). Here, we
436 used magnetic modeling of these anomalies to characterize NRM directions and intensity of selected discrete
437 grains.

3.4.1 MAGNETIC DATA AND PROCESSING

438 Isolated magnetic anomalies are observed in all magnetic scans (Fig. 5) associated with the opaque mineralogy.
439 Here we model three grains, one for each thin section, which correlate with strong dipolar anomalies (Fig. 9a, b
440 and c). For each grain the magnetic anomaly and analytic signal maps are compared and shown overlaying the
441 optical scan in Fig. 9. The analytic signal of the magnetic field was calculated to locate and distinguish among
442 multiple sources contributing to each dipolar anomaly. This field transformation, obtained through a combination
443 of the horizontal and vertical gradients of the magnetic field, does not depend on the direction of magnetization of
444 the anomaly source, but depends on its location and shape. Assuming a rectangular, or Cartesian, coordinate
445 system with the top plane of the thin section in the xy-plane and with the z-axis (measurement direction)
446 perpendicular to it and directed downward into the thin section, we calculated the analytic signal of the vertical
447 magnetic field (B_z). The amplitude of the analytic signal at (x,y) is calculated as the square root of the sum of the
448 squares of the derivatives in the x, y, and z directions of the magnetic field B_z according to (Roest et al., 1992):

449

$$(1) \quad |AS(x,y)| = \sqrt{\left(\frac{\partial Bz}{\partial x}\right)^2 + \left(\frac{\partial Bz}{\partial y}\right)^2 + \left(\frac{\partial Bz}{\partial z}\right)^2}$$

450

Considering the high aspect ratio of our modeled grains, the analytic signal amplitude should have a maximum

451

centered above the magnetic source (Nabighian 1972). A comparison between the analytic signal and grain shapes

452

shows that:

453

- For the grain in Fig. 9d, the analytic signal reflects the shape of the left side of the grain and indicates that

454

region as the main source of the magnetic anomaly.

455

- For the grain in Fig. 9e, the analytic signal is dominantly centered over the grain with smaller highs

456

towards the left side of the grain that could reflect compositional variations.

457

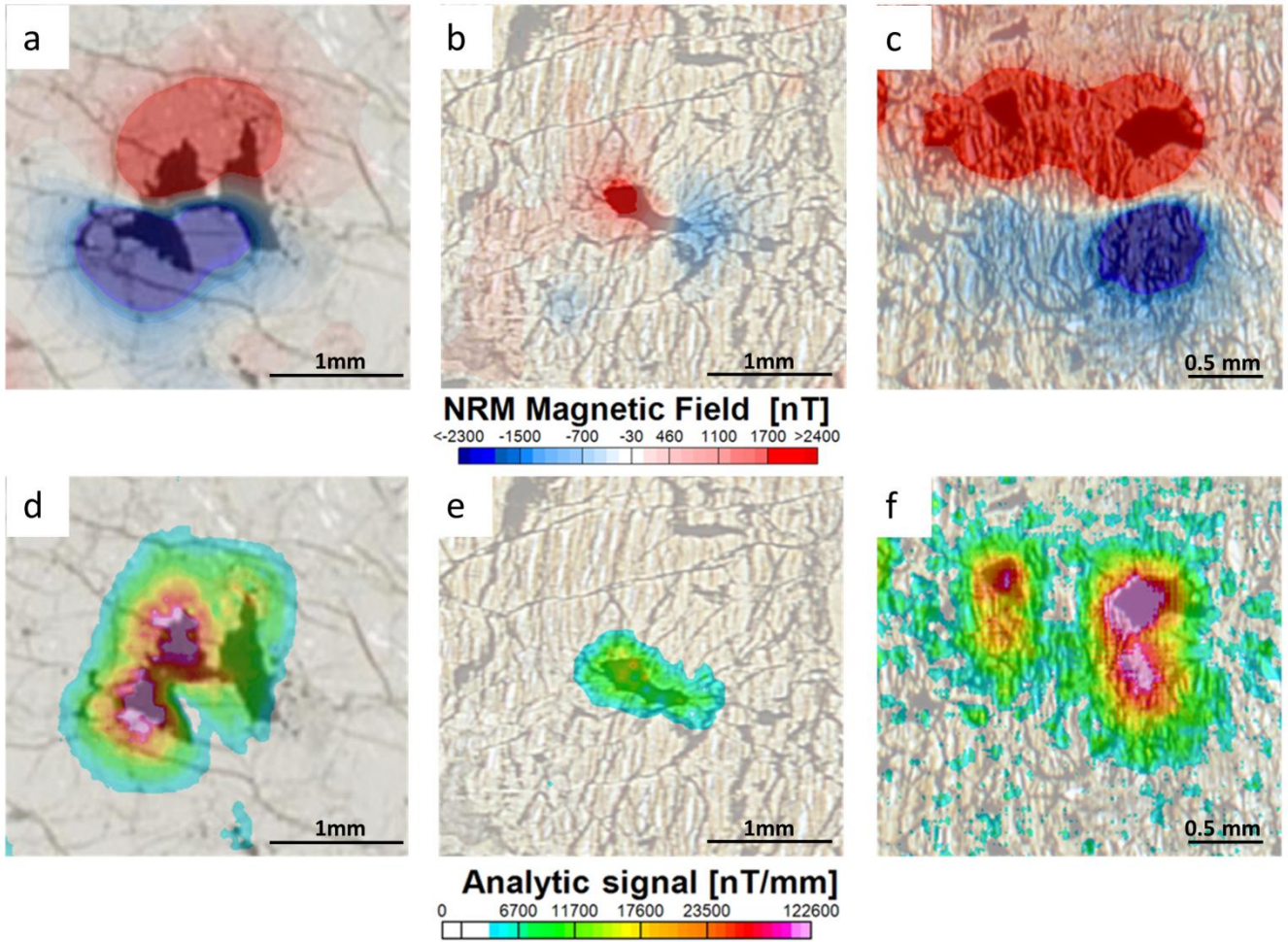
- For the grain in Fig. 9f, there are three different highs in the analytic signal, which can be distinguished,

458

two correlating with large opaque grains, and one below one of the large grains. This may indicate an

459

additional source of fine magnetite within the serpentized veins.



460

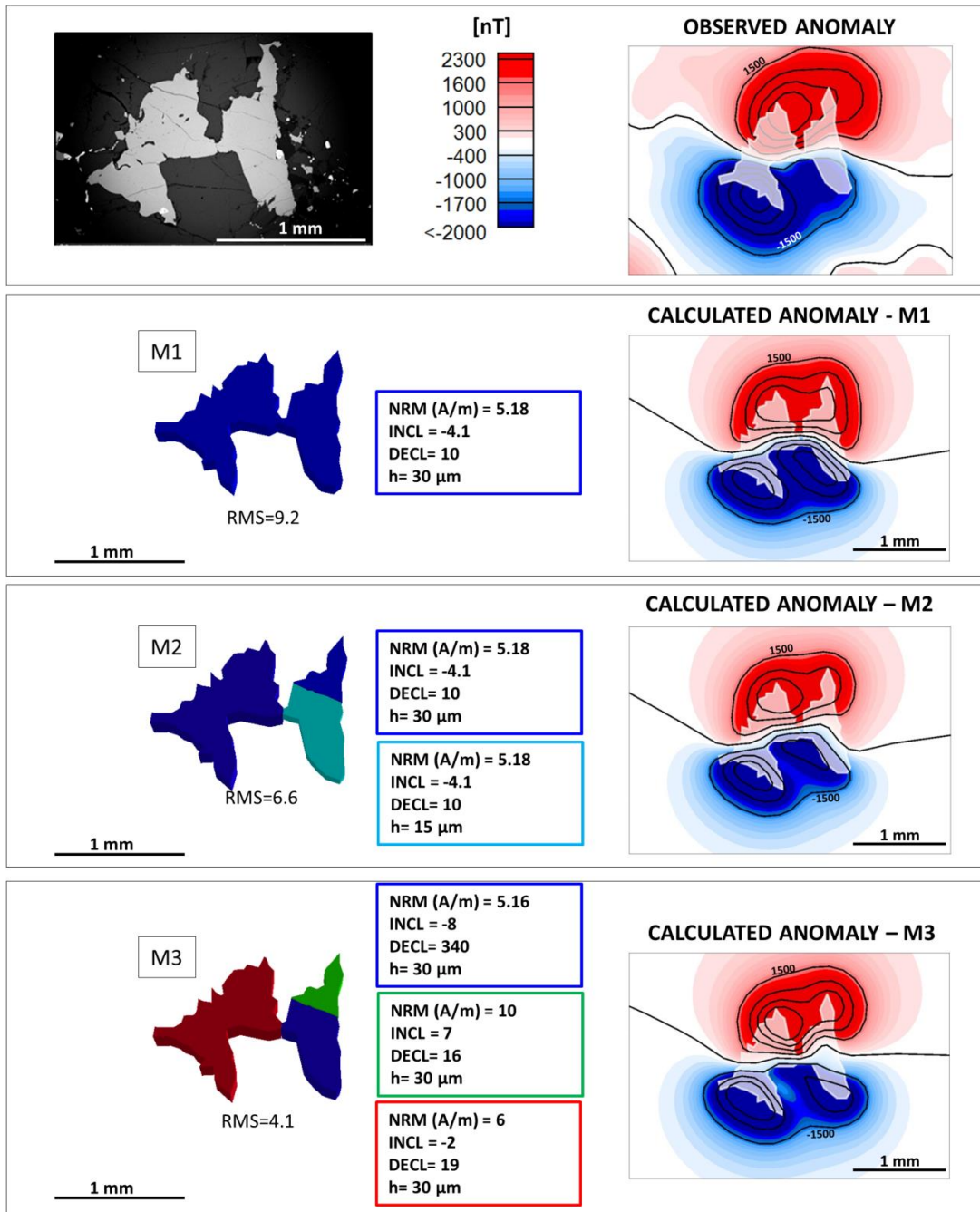
461 *Fig. 9. Magnetic anomaly maps (top) and analytic signal maps (bottom) for three selected grains. Displayed*
 462 *grains are from CS4 (left), 15S2D (middle) and 15S2B (right) thin sections. Grains locations are indicated*
 463 *in Fig. 5 with black boxes labelled as a^1 , b^2 and c^2 . These show the respective grain location within each thin*
 464 *section respectively.*

3.4.2 REMANENT MAGNETIZATION MODELING AND RESULTS

465 We modeled the NRM intensity and direction of the three grains shown in Fig. 9, using a forward modeling
 466 approach with Model Vision. Modeling of each grain was made using homogeneously magnetized 3D frustum
 467 bodies with top and bottom constrained to be horizontal and defined by polygons, or tabular bodies with a
 468 maximum thickness of 30 μ m (thin section thickness). Each body was then inverted for magnetization intensity

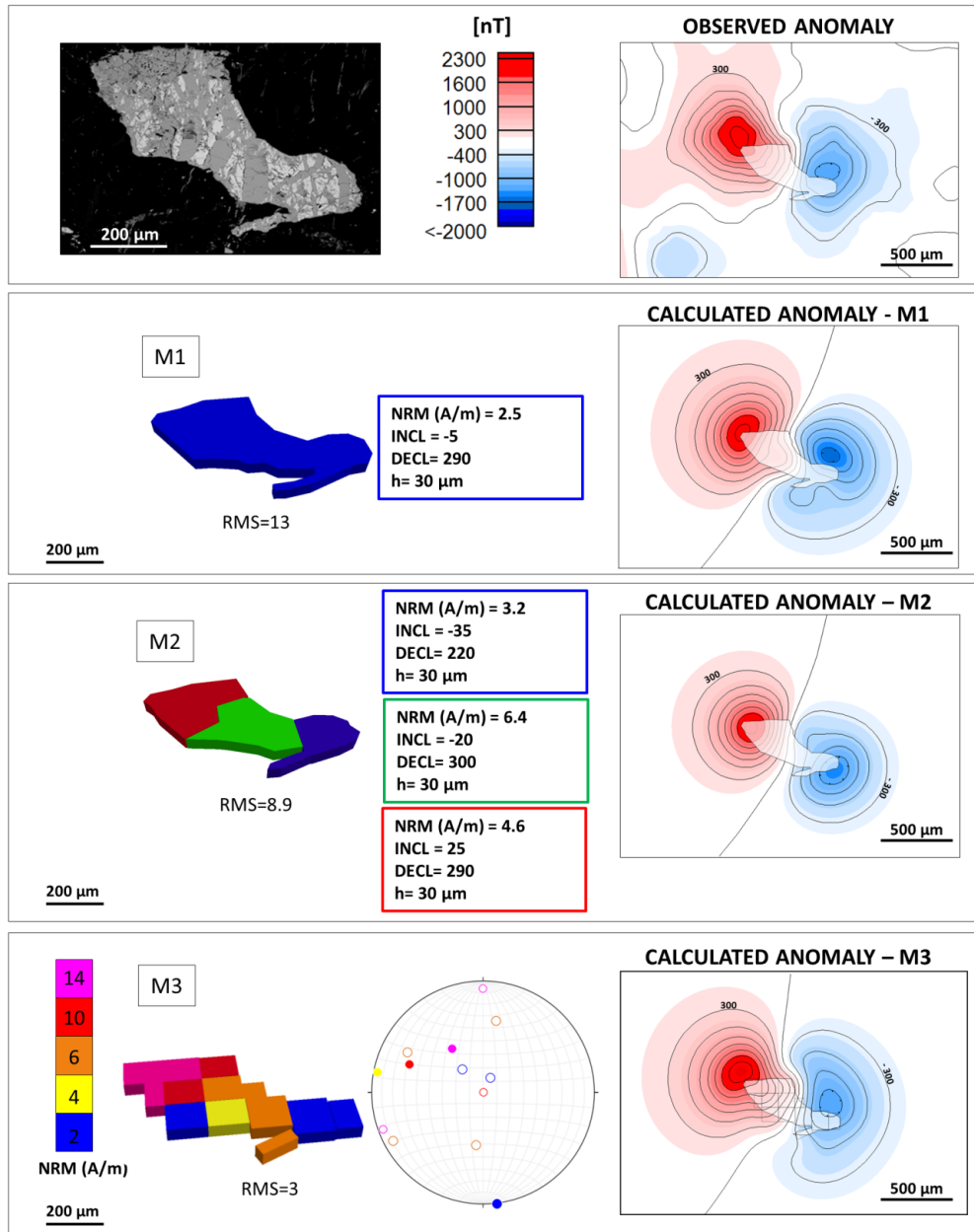
469 and direction to obtain the best fit between observed and calculated anomaly field. Several tests were made on
470 selected grains. The best fitting models, for each test, are shown in Figs. 10, 11 and 12, with their respective
471 modeling parameters. Modeling tests for a Cr-spinel grain from CS4 (Figs. 2a&5a) are shown in Fig. 10. Three
472 different tests have been run (M1, M2 and M3). The first test considers a single large homogeneously magnetized
473 grain, whose shape is constrained by the SEM images and by the thin section thickness of 30 μ m. Inversions for
474 magnetization intensities and direction gave a percentage root mean square error (RMS) of 9.2 for the best fitting
475 model (M1). The RMS is expressed as a percentage of the dynamic range of the active data. It is calculated, for all
476 positions at which the field values are used in the inversion, as the root mean square difference between the model
477 input and output field values at a specific point, divided by the total range of the input magnetic field data in the
478 modeled area. The second test was made using two sub-grains with same magnetization intensities and direction
479 as in the M1 model, and inverting only for vertical extents of the two sub-grains and limiting this extent to a
480 maximum of 30 μ m. This test gave a lower RMS error of 6.6; the best fitting model M2 requires a lower thick-ness
481 for the sub-grain to the right of the larger grain. The third test was made assuming three sub-grains of fixed
482 thickness (30 μ m) and freely variable magnetization intensity and directions. The best fitting model gave a RMS
483 error to the observed anomaly of 4.1 and suggests a variable intensity of the remanent magnetization within the
484 modeled grain, but broadly similar magnetization directions. For the magnetite grain with an intergrowth of
485 pentlandite from 15S2D (Fig. 5b) three modeling tests were run and the best fitting models are shown in Fig. 11.
486 Model M1 assume a homogeneously magnetized grain and gave a RMS error of 13. In model M2 the grain is
487 subdivided in three smaller grains with same vertical extent but freely variable remanent magnetization intensities
488 and directions; the model gave a RMS error to the observed anomaly of 8.9. In the last model M3 the modeled
489 grain is subdivided in multiple tabular bodies, each one homogeneously magnetized, which are inverted to obtain
490 the best fit between the observed and the calculated anomaly. The model M3 gave a RMS error of 3 and similar to
491 the grain in CS4 suggests multiple sources of magnetization within the larger grains with higher intensities on the
492 right side of the grain. This can be explained by variations in the amount of magnetite versus pentlandite. The
493 stereoplot in Fig. 11 shows the magnetization direction of each sub-grain, which indicates extremely variable
494 magnetization within the composite particle. Two grains from the serpentinized thin section 15S2B were modeled

495 (Fig. 12). The opaque grains are magnetite intergrown with pentlandite, pyrrhotite, and minor chalcopyrite. Two
496 tests were performed: the first test assumes the two grains are homogeneously magnetized, and that the two larger
497 grains are the main source of the observed anomalies. The second test (analogously to the M3 in the previous
498 modeled grains) inverts a set of tabular bodies for remanent magnetization direction and intensity. The best fitting
499 model in the first test gave a RMS error of 14 with a notable mismatch on the right side of the modeled area. This
500 test suggests that an important source of magnetization is located below the large grain to the right of the modeled
501 area, which is reversely magnetized (black box in Fig. 12). In reflected light, at high magnification, smaller
502 magnetite grains (up to 10 μ m) are visible on the surface of the thin section, and additional particles are likely
503 below the surface of the sample. This area has been modeled in the second test by mean of tabular bodies, which
504 gave a localized NRM intensity of 12 A/m, and steep negative inclination and an improved RMS error of 5.
505 Modeling of the magnetic anomalies over the three isolated grains in the thin section indicates heterogeneous
506 sources of remanent magnetization with intensities varying between 2 and 12 A/m and variable directions. In the
507 CS4 sample this variability may be associated with a variable amount of small ferrichromite exsolved within the
508 hosting Cr- spinel. In the two serpentized thin sections generally weaker NRMs correlate with a larger amount
509 of pentlandite versus magnetite. In these samples the magnetization was acquired when magnetite was produced
510 during serpentization at lower temperature than the blocking temperature. The variable direction of the NRMs
511 may also reflect the multidomain behavior expected for such large grains, which results in a less efficient
512 acquisition of the magnetization.



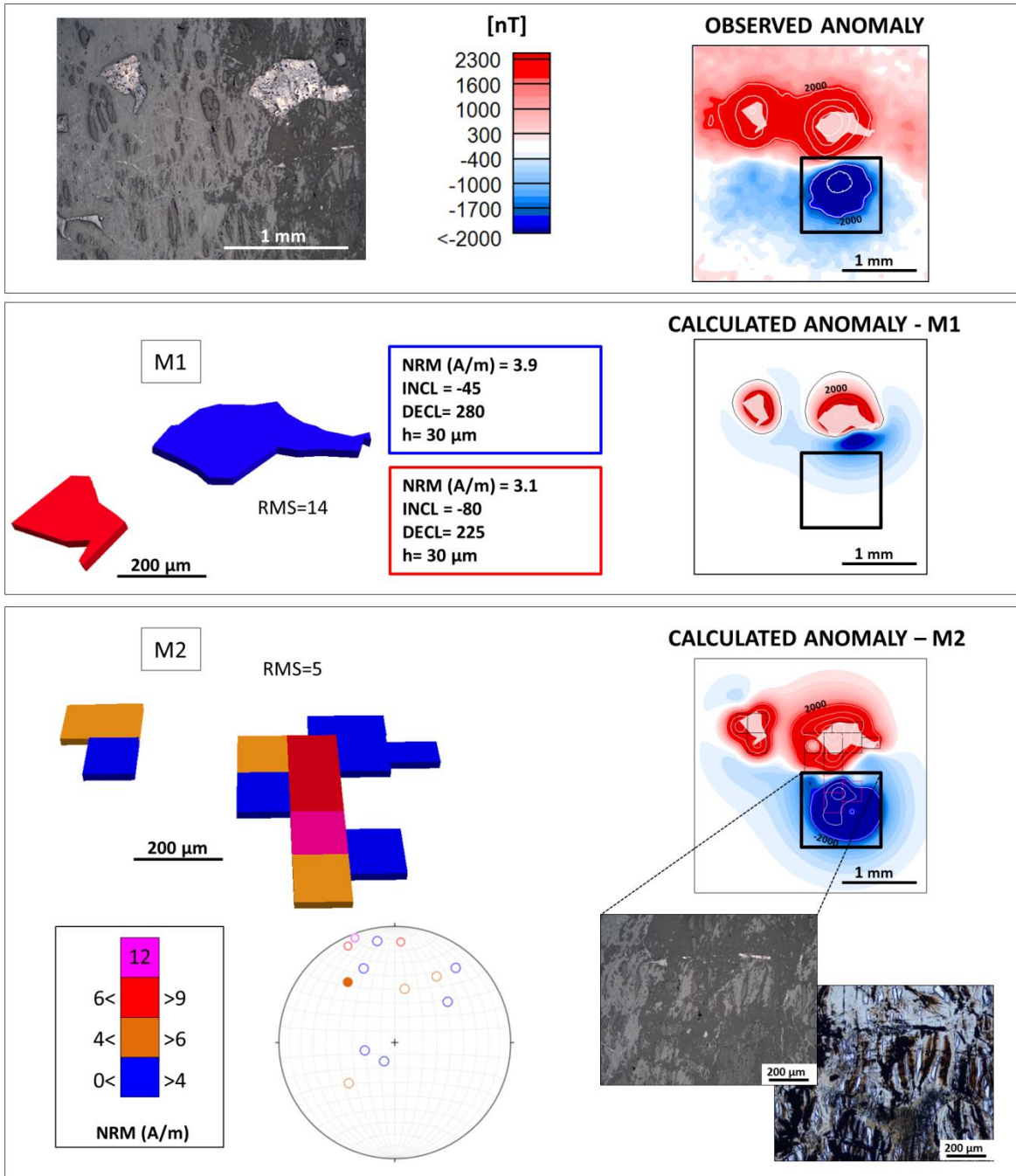
513

514 *Fig. 10. NRM modeling tests for CS4 grain. Top panel: SEM image of the modeled Cr-spinel grain and*
 515 *correlative magnetic anomaly. Below for each test are: 3D image of the grain color coded by number of bodies*
 516 *used in the modeling (left) and respective modeling parameters (center) and resulting calculated anomaly*
 517 *(right) with contours interval of 1500 nT. RMS =root means square error between calculated and observed*
 518 *anomaly grids.*



519

520 *Fig. 11. NRM modeling test results for 15S2D grain. Top an SEM image of the modeled grain. For each test*
 521 *there is a panel with 3D image of the grain color coded by number of bodies used in the modeling (left) and*
 522 *respective modeling parameters (center) and resulting calculated anomaly (right) with contours interval of 300*
 523 *nT. RMS = root means square error between calculated and observed anomaly grids. The stereoplot in the M3*
 524 *model is for NRM directions of the modeled tabular bodies; closed circles are for positive inclinations and open*
 525 *circles for negative inclinations, colors are for NRMs intensities.*



526

527 *Fig. 12. NRM modeling tests for 15S2B grain. Above are reflected light image of the modeled grains and*
 528 *measured anomaly. Below (for each test) are: 3D image of the grain color coded by number of bodies used in*
 529 *the modeling (left) and respective modeling parameters (center) and resulting calculated anomaly (right) with*
 530 *contours interval of 2000 nT. RMS = root means square error between calculated and observed anomaly grids.*

531 *The stereoplot in the M2 model is for NRM directions of the modeled tabular bodies; closed circles are for*
532 *positive inclinations and open circles for negative inclinations, circles' colors indicate NRM intensities*

4. DISCUSSION

533 We investigated three samples of the Reinfjord Ultramafic Complex using rock magnetic methods, optical and
534 electron microscopy and magnetic modeling. The bulk susceptibility and NRM of the serpentinized and pristine
535 dunite samples vary by more than one order of magnitude. These properties were investigated with respect to the
536 magnetic mineralogy, composition, fabric and texture. Magnetic scans of thin sections were used to locate the
537 magnetic sources that result in distinct magnetic anomalies. We have shown that the magnetic mineralogy, the
538 source of the magnetic anomalies, is significantly different in the pristine and serpentinized dunite samples. In the
539 pristine dunite sample, where the primary magnetic mineralogical assemblage is preserved, the predominant
540 source is Cr-spinel with fine exsolution microstructures (1–3 μ m) of iron-rich ferrichromite to end-member
541 magnetite. The Cr-spinel host is paramagnetic at room temperature due to its composition, therefore the
542 exsolution intergrowths are the source of the magnetic anomalies. Thermomagnetic experiments confirm that
543 there is a compositional variation within the grains which is reflected in the wide T_c temperature range between
544 200 °C and 579 °C (Table 3). The Verwey transition in the temperature versus susceptibility curves indicates the
545 presence of near end-member magnetite. By contrast the predominant magnetic carrier in the serpentinized
546 samples is end-member magnetite. Hysteresis parameters on the CS4 sample indicates that the bulk signal is a
547 mixture of pseudo-single domain and single-domain size grains with relatively high coercivity, which can be
548 explained by the presence of fine exsolution blebs. These are not homogeneously distributed within the Cr-spinel
549 grains and likely the cause of the heterogeneous sources of magnetization shown in the analytic signal map and in
550 the modeling results. Our modeling results confirm the microscopic observation of stronger magnetic intensity in
551 areas of greater occurrences of ferrichromite exsolution within the Cr-rich spinel and weaker intensity where these
552 exsolved phases were not observed. In the serpentinized dunite thin sections, the largest anomalies correlate with
553 larger grains of magnetite commonly found together with pentlandite or other sulfides. Thermal experiments

554 indicate magnetite is the main magnetic carrier in the sample. Characteristic features which indicate magnetite, are
555 the well-defined Hopkinson peaks and Verwey transitions, observed in the temperature-susceptibility curves, and
556 the T_c estimates close to the T_c of endmember magnetite. The magnetite in veins, observed at the SEM, is fine
557 grained, in agreement with the hysteresis parameters (M_r/M_s and H_{cr}/H_c) approaching values that are diagnostic
558 of very fine single-domain particles. Most of the fine magnetite grains have a relatively small effect on the
559 observed magnetic scans' anomalies. This is possibly related to the resolution of the magnetic scans; lowering the
560 sensor height and increasing the sampling density could better resolve the sources of the magnetization but this
561 has instrumental challenges. It is also possible that, although the field intensity is weaker on the magnetic scan,
562 the sources of these anomalies may contribute to the bulk properties if they preserve a consistent magnetization
563 direction throughout the sample. Here, we modeled only the anomalies caused by larger grains that are associated
564 with the highest field intensities. Most of the fine-grained magnetite in the serpentinized samples formed during
565 serpentinization and, as suggested by the ratio between NRM and M_r (Table 2), yields a lower efficiency of
566 magnetization with respect to the magnetic carriers in the pristine dunite sample. The Cr-spinel in the dunite likely
567 developed the magnetic Fe-rich exsolution microstructures when cooling through the solvus at temperatures near,
568 or above their respective T_c , therefore the NRM in this sample can be considered a thermoremanent
569 magnetization (TRM). For non-interacting single-domain particles, Stacey and Banerjee (1974) calculate that
570 remanence acquired during growth through chemical alteration (e.g. during serpentinization), a chemical remanent
571 magnetization (CRM), must be smaller than the TRM of the same particles. While a similar calculation cannot be
572 made for grains with other domain states, which are common in natural samples, Smirnov and Tarduno (2005)
573 argue that the CRM of particles with other domain states is likely to be even weaker than those that are single-
574 domain. This suggests that magnetization acquired during serpentinization (hereb400 °C) must have a lower
575 efficiency than a TRM, consistent with our observations on the efficiency of pristine dunite and serpentinite
576 samples. Modeling of the large discrete magnetic grains in the serpentinized samples confirms the microscopic
577 observation of stronger magnetic intensity in areas of discrete magnetite, and weaker intensity where magnetite is
578 found together with pentlandite, or other sulfides (chalcopyrite and pyrrhotite). The orientation of the magnetic
579 anomalies varies across these thin sections and in future work this variation could be tied to the magnetic history,

580 or the stability of NRM and acquisition of recent magnetic components. Such lines of enquiry could provide
581 information on the timing of the serpentinization reactions. Scanning magnetic microscopy could be used to
582 distinguish between primary and later magnetite formed during serpentinization, by measuring the magnetization
583 response of individual, or assemblages of grains.

584 To summarize, modeling of the magnetic anomalies over isolated grains indicated heterogeneous sources of NRM
585 within the grains in serpentinite with intensities varying from 2 to 14 A/m and variable directions. These estimates
586 are slightly higher for the serpentinized sample grains than in the pristine dunite. This result together with the
587 composition, the percentage of magnetic minerals and the fine-grainsize of the magnetic material in the
588 serpentinized sample explain its high bulk magnetic susceptibility and NRM.

5. CONCLUSIONS

589 Scanning magnetic microscopy was used here to map the magnetic mineralogy of serpentinized and pristine
590 dunite samples. Magnetic modeling in combination with chemical and magnetic properties analyses allowed
591 characterization of the main magnetic carriers. The main results are summarized below:

- 592 • Magnetic carriers were identified based on Curie temperatures estimates and microscopic observations. In the
593 serpentinized samples the magnetic carriers are end-member magnetite found both in veins, and as discrete
594 large grains. Minor pyrrhotite was also observed. In the pristine dunite sample, the magnetic carriers are
595 exsolution blebs with ferrichromite to end-member magnetite compositions in the Cr-spinel grains.
- 596 • The bulk NRM and magnetic susceptibility values are one order magnitude lower in the dunite sample than the
597 serpentinized samples. This is explained by differences in magnetic mineralogy, content, grain size and texture
598 between the serpentinized and the dunite samples. In the dunite sample the percentage of magnetic minerals
599 calculated from M_s values is approximately 0.2%. Here, ferrichromite and minor magnetite exsolution
600 microstructures in the Cr-spinel contribute to the magnetization. In the serpentinized sample the percentage of
601 magnetic oxides is significantly larger at 2.8%, as calculated from M_s . Hysteresis properties indicate that the
602 magnetite grains range from single domain to pseudo-single domain in size.

- 603 • Detailed modeling of a magnetic anomaly over an isolated grain indicates that there are heterogeneous sources
604 of magnetic direction and intensity within the grain, in both pristine and serpentinized dunite samples.
- 605 • In the pristine dunite sample the heterogeneity is limited to the magnetization intensity which we interpret to
606 be caused by variable concentration and composition of the ferrichromite exsolution within the Cr-spinel.
607 However, the direction of magnetization is similar through-out the grain, implying similar timing of
608 acquisition of magnetization for the exsolution microstructures.
- 609 • In the anomaly modeled over the serpentinized sample this heterogeneity applies both to the intensity and
610 direction of the magnetization.
- 611 • Evaluating a larger view of the magnetic scan of the pristine dunite sample shows dipolar anomalies of similar
612 orientation across the entire thin section. This suggests a consistent magnetization direction and may imply that
613 the bulk magnetization direction of the sample is consistent with the fine-scale magnetization mapped here,
614 and that this was acquired during initial cooling through the magnetite–Cr-spinel solvus, after emplacement. In
615 the serpentinized samples the scans show variability in the orientation of the large dipolar anomalies among
616 the different magnetite grains in the thin section. This heterogeneity will lower the total NRM. However, the
617 fine-grained magnetite located in the veins will also add to the NRM. Future work would include
618 demagnetization of the thin sections followed by magnetic mapping. This could be used to investigate the
619 stability of the magnetization, and to explain better the non-unidirectional magnetization in the serpentinized
620 samples.

621 We conclude that the bulk magnetic properties of these samples can be explained by the observed magnetic
622 mineralogy. Forward modeling was effective in defining areas of higher magnetization that was constrained by
623 the 3D geometry of the magnetic grains. Serpentinization clearly affected the heterogeneity of the magnetization
624 direction across the thin section. The observation of numerous anomalies with variable directions and intensities
625 over the larger grains in the magnetic scans of the serpentinites may suggest that the magnetization was acquired
626 over a long time interval. In order to investigate further the link between the bulk NRM and the magnetization of
627 the discrete grains, modeling of the entire thin section should be made. Curvature analysis (Phillips et al., 2007) of

628 the magnetic data acquired by scanning magnetic microscopy could be used to automatically determine the
629 boundaries of magnetic sources across the entire thin section. This is planned for future work.

630 **ACKNOWLEDGMENTS**

631 We thank the editors Bjørn Jamtveit and Marguerite Godard, and the two anonymous reviewers in addition to
632 Peter Robinson, Alexander Michels, Richard Blakely and Hajo Götze for constructive comments. The research
633 leading to these results was funded by People Programme (Marie Curie Actions) of the European Union's Seventh
634 Framework Programme FP7/2007-2013/under REA – Grant Agreement n° 608001. The Research Council of
635 Norway is acknowledged for the support to the Norwegian Micro- and Nano-Fabrication Facility, NorFab, project
636 number 245963/F50, and development of the scanning magnetic microscope (NFR grant 222666). Scanning
637 SQUID microscopy was conducted during the visit of S.A. McEnroe to GSJ/AIST supported by JSPS invitation
638 fellowship (S16128). Ayako Katayama is thanked for the help in measurement of scanning SQUID microscopy.
639 We further thank Andrea Risplendente for his technical assistance at the microprobe.

640

641 Appendix A. Characteristic hysteresis parameters on sample chips before (BH) and after (AH) high temperature
 642 VSM experiments. The precision used in the table is significant.

Sample	Chip	Chip Mass [g]	Mr [Am ² /kg]	Ms [Am ² /kg]	Hc	Hcr	Mr/Ms	Hcr/Hc	
CS4	C4	0.11	0.03	0.15	12.0	42.8	0.19	3.57	BH
		0.11	0.03	0.14	12.4	41.1	0.18	3.31	AH
	C5	0.09	0.03	0.10	17.8	36.2	0.28	2.03	BH
		0.09	0.03	0.10	17.5	33.4	0.27	1.91	AH
15S2	D4	0.06	1.58	4.56	29.4	41.8	0.35	1.42	BH
		0.06	1.28	4.21	24.8	37.4	0.30	1.51	AH
	D5	0.06	2.48	6.15	29.6	40.8	0.40	1.38	BH
		0.06	2.06	5.60	24.1	33.4	0.37	1.39	AH
	B3	0.07	2.30	6.49	32.0	45.5	0.36	1.42	BH
		0.07	1.63	5.65	25.8	40.8	0.29	1.58	AH

643

6. REFERENCES

- 644 Barnes, S.J., Roeder, P.L., 2001. The range of spinel compositions in terrestrial mafic and ultramafic rocks.
645 *Journal of Petrology* 42, 2279-2302.
- 646 Church, N., McEnroe, S., 2018. Magnetic Field Surveys of Thin Sections. DOI:0.1071/ASEG2018abW10_3F
- 647 Clark, D.A., 1997. Magnetic petrophysics and magnetic petrology: aids to geological interpretation of magnetic
648 surveys. *AGSO Journal of Australian Geology and Geophysics* 17, 83-104.
- 649 Day, R., Fuller, M., Schmidt, V., 1977. Hysteresis properties of titanomagnetites: grain-size and compositional
650 dependence. *Physics of the Earth and planetary interiors* 13, 260-267.
- 651 Domenichini, B., Amilain-Basset, K., Bourgeois, S., 2002. Dynamic segregation during ferrite oxidation revealed
652 by XPS. *Surface and interface analysis* 34, 527-530.
- 653 Dunlop, D.J., 2002. Theory and application of the Day plot (Mrs/Ms versus Hcr/Hc) 1. Theoretical curves and
654 tests using titanomagnetite data. *Journal of Geophysical Research: Solid Earth* 107.
- 655 Dunlop, D.J., Özdemir, Ö., 1997. *Rock magnetism: Fundamentals and Frontiers*. Cambridge university press.
- 656 Fabian, K., Shcherbakov, V.P., McEnroe, S.A., 2013. Measuring the Curie temperature. *Geochem.*
657 *Geophys.Geosyst.* 14, 947–961.
- 658 Francombe, M., 1957. Lattice changes in spinel-type iron chromites. *Journal of Physics and Chemistry of Solids*
659 3, 37-43.
- 660 Fu, R.R., Lima, E.A., & Weiss, B.P. (2014). No nebular magnetization in the Allende CV carbonaceous
661 chondrite. *Earth and Planetary Science Letters*. *Earth and Planetary Science Letters*, 404(C), 54–66.
662 <http://doi.org/10.1016/j.epsl.2014.07.014>

663 Fukuzawa, T., Nakamura, N., Oda, H., Uehara, M., Nagahama, H., 2017. Generation of billow-like wavy folds by
664 fluidization at high temperature in Nojima fault gouge: microscopic and rock magnetic perspectives. *Earth,*
665 *Planets and Space* 69, 54.

666 Funaki, M., Tunyi, I., Orlický, O., Porubcan, V., 2000. Natural remanent magnetization of Rumanova chondrite
667 (H5) acquired by the shock metamorphisms S3. *Antarctic meteorite research* 13, 78.

668 Grannes, K.R.B., 2016. Cryptic Variations of Olivene and Clinopyroxene in the RF-4 Drill-Core:-A Geochemical
669 study of the Reinford Ultramafic Complex, Norway. NTNU.

670 Hankard, F., Gattacceca, J.m., Fermon, C., Pannetier-Lecoeur, M., Langlais, B., Quesnel, Y., Rochette, P.,
671 McEnroe, S.A., 2009. Magnetic field microscopy of rock samples using a giant magnetoresistance-based
672 scanning magnetometer. *Geochemistry, Geophysics, Geosystems* 10.

673 Harrison, R.J., Putnis, A., 1996. Magnetic properties of the magnetite-spinel solid solution: Curie temperatures,
674 magnetic susceptibilities, and cation ordering. *Mineralogical Society of America*.

675 Horen, H., Soubrand, M., Kierczak, J., Joussein, E., Néel, C., 2014. Magnetic characterization of ferrichromite in
676 soils developed on serpentinites under temperate climate. *Geoderma* 235, 83-89.

677 Kądziałko-Hofmokr, M., Delura, K., Bylina, P., Jeleńska, M., Kruczyk, J., 2008. Mineralogy and magnetism of
678 Fe-Cr spinel series minerals from podiform chromitites and dunites from Tapadla (Sudetic ophiolite, SW Poland)
679 and their relationship to palaeomagnetic results of the dunites. *Geophysical Journal International* 175, 885-900.

680 Kawai, J., Oda, H., Fujihira, J., Miyamoto, M., Miyagi, I., Sato, M., 2016. SQUID microscope with hollow-
681 structured cryostat for magnetic field imaging of room temperature samples. *IEEE Transactions on Applied*
682 *Superconductivity* 26, 1-5.

683 Larsen, R.B., Grant, T., Sørensen, B.E., Tegner, C., McEnroe, S., Pastore, Z., Fichler, C., Nikolaisen, E., Grannes,
684 K.R., Church, N., 2018. Portrait of a giant deep-seated magmatic conduit system: the Seiland Igneous Province.
685 *Lithos* 296, 600-622.

686 Lima, E.A., Bruno, A.C., Carvalho, H.R., Weiss, B.P., 2014. Scanning magnetic tunnel junction microscope for
687 high-resolution imaging of remanent magnetization fields. *Measurement Science and Technology* 25, 105401.

688 McEnroe, S.A., Brown, L.L., Robinson, P., 2009a. Remanent and induced magnetic anomalies over a layered
689 intrusion: Effects from crystal fractionation and magma recharge. *Tectonophysics* 478, 119-134.

690 McEnroe, S.A., Fabian, K., Robinson, P., Gaina, C., Brown, L.L., 2009b. Crustal magnetism, lamellar magnetism
691 and rocks that remember. *Elements* 5, 241-246.

692 McEnroe, S.A., Robinson, P., Miyajima, N., Fabian, K., Dyar, D., Sklute, E., 2016. Lamellar magnetism and
693 exchange bias in billion-year-old titanohematite with nanoscale ilmenite exsolution lamellae: I. Mineral and
694 magnetic characterization. *Geophysical Journal International* 206, 470-486.

695 McEnroe, S.A., Robinson, P., Church, N., Purucker, M., 2018. Magnetism at Depth: A View from an Ancient
696 Continental Subduction and Collision Zone. *Geochemistry, Geophysics, Geosystems* 19, 1123-1147.

697 Minyuk, P., Subbotnikova, T., Brown, L., Murdock, K., 2013. High-temperature thermomagnetic properties of
698 vivianite nodules, Lake El'gygytyn, Northeast Russia. *Climate of the Past* 9, 433.

699 Nabighian, M.N., 1972. The analytic signal of two-dimensional magnetic bodies with polygonal cross-section: its
700 properties and use for automated anomaly interpretation. *Geophysics* 37, 507-517.

701 Noguchi, A., Oda, H., Yamamoto, Y., Usui, A., Sato, M., Kawai, J., 2017. Scanning SQUID microscopy of a
702 ferromanganese crust from the northwestern Pacific: Sub-millimeter scale magnetostratigraphy as a new tool for
703 age determination and mapping of environmental magnetic parameters. *Geophysical Research Letters* 44, 5360-
704 5367.

705 Oda, H., Kawai, J., Miyamoto, M., Miyagi, I., Sato, M., Noguchi, A., Yamamoto, Y., Fujihira, J.-i., Natsuhara,
706 N., Aramaki, Y., 2016. Scanning SQUID microscope system for geological samples: system integration and initial
707 evaluation. *Earth, Planets and Space* 68, 179.

708 Oda, H., Usui, A., Miyagi, I., Joshima, M., Weiss, B.P., Shantz, C., Fong, L.E., McBride, K.K., Harder, R.,
709 Baudenbacher, F.J., 2011. Ultrafine-scale magnetostratigraphy of marine ferromanganese crust. *Geology* 39, 227-
710 230.

711 Petersen, N., Bleil, U., 6.2.5 Curie temperature: Datasheet from Landolt-Börnstein - Group V Geophysics ·
712 Volume 1B: "Subvolume B" in SpringerMaterials (https://dx.doi.org/10.1007/10201909_76), in: Angenheister, G.
713 (Ed.). Springer-Verlag Berlin Heidelberg.

714 Phillips, J.D., Hansen, R.O., Blakely, R.J., 2007. The use of curvature in potential-field interpretation. *Exploration*
715 *Geophysics* 38, 111-119.

716 Puranen, R. (1989), *Susceptibilities, Iron and Magnetite Content of Precambrian Rocks in Finland*, 90 ed.,
717 Geological Survey of Finland, Report of Investigation.

718 Readman, P., and W. O'Reilly, 1972. Magnetic properties of oxidized (cation-deficient) titanomagnetites (Fe, Ti,
719 block) 304, *Journal of Geomagnetism and Geoelectricity*, 24(1), 69-&. (O'Reilly did a huge amount of work on
720 effect of oxidation state).

721 Robbins, M., Wertheim, G., Sherwood, R., Buchanan, D., 1971. Magnetic properties and site distributions in the
722 system $\text{FeCr}_2\text{O}_4\text{-Fe}_3\text{O}_4$ ($\text{Fe}^{2+} \text{Cr}^{2-x}\text{Fe}^{3+x}\text{O}_4$). *Journal of Physics and Chemistry of Solids* 32, 717-729.

723 Robinson, P., McEnroe, S., Miyajima, N., Fabian, K., Church, N., 2016. Remanent magnetization, magnetic
724 coupling, and interface ionic configurations of intergrown rhombohedral and cubic Fe-Ti oxides: a short survey.
725 *American Mineralogist* 101, 518-530.

726 Roest, W.E., Verhoef, J., Pilkington, M., 1992, Magnetic interpretation using 3-D analytic signal: *Geophysics*, 57,
727 116-125.

728 Smirnov, A. V., and J. A. Tarduno (2005), Thermochemical remanent magnetization in Precambrian rocks: Are
729 we sure the geomagnetic field was weak?, 110(B6), B06103, doi:10.1029/2004JB003445.

730 Stacey, F. D., and S. K. Banerjee (1974), *The Physical Principles of Rock Magnetism*, Elsevier Scientific
731 Publishing Company.

732 Tauxe, L., 1998. *Paleomagnetic Principles and Practice*, Kluwer, New York.

733 Thomas, I.M., Moyer T.C., and Wikswo J.P. Jr. (1992), High resolution magnetic susceptibility imaging of
734 geological thin sections: pilot study of a pyroclastic sample from the Bishop Tuff, California, U.S.A, *Geophys*
735 *Res Lett*, 19(21), 2139–2142, doi:10.1029/92GL02322.

736 Tominaga, M., Beinlich, A., Lima, E.A., Tivey, M.A., Hampton, B.A., Weiss, B., Harigane, Y., 2017. Multi-scale
737 magnetic mapping of serpentinite carbonation. *Nature Communications* 8, 1870.

738 Walz, F., The Verwey transition - a topical review, *J Phys-Condens Mat*, 14(12), (2002), R285–R340,
739 doi:10.1088/0953-8984/14/12/203.

740 Weiss, B.P., Kirschvink, J.L., Baudenbacher, F.J., Vali, H., Peters, N.T., Macdonald, F.A., Wikswo, J.P., 2000. A
741 low temperature transfer of ALH84001 from Mars to Earth. *Science* 290, 791-795.

742 Weiss, B.P., Lima, E.A., Fong, L.E., Baudenbacher, F.J., 2007. Paleomagnetic analysis using SQUID microscopy.
743 *Journal of Geophysical Research: Solid Earth* 112.

744 Weiss, B.P., Fong, L.E., Vali, H., Lima, E.A., & Baudenbacher, F.J. (2008). Paleointensity of the ancient Martian
745 magnetic field. *Geophysical Research Letters*, 35(23), L23207. doi:10.1029/2008GL035585, 2008.

746 Weiss, B.P., Vali, H., Baudenbacher, F.J., Kirschvink, J.L., Stewart, S.T., Shuster, D.L., 2002. Records of an
747 ancient Martian magnetic field in ALH84001. *Earth Planet. Sci. Lett.* 201, 449–463.

